2017

MASSIVE MIMO PERFORMANCE ANALYSIS AND RADAR SENSOR NETWORKS BASED TARGET DETECTION

Ganlin Zhao

MASSIVE MIMO PERFORMANCE ANALYSIS AND RADAR SENSOR NETWORKS BASED TARGET DETECTION

by

GANLIN ZHAO

Presented to the Faculty of the Graduate School of

The University of Texas at Arlington in Partial Fulfillment

of the Requirements

for the Degree of

DOCTOR OF PHILOSOPHY

THE UNIVERSITY OF TEXAS AT ARLINGTON

Nov 2017

To my family.

ACKNOWLEDGEMENTS

Firstly, I would like to thank my supervisor, Dr. Qilian Liang, for constantly motivating and encouraging me, and also for his helpful advice during the course of my doctoral studies. His enthusiasm and attitude toward research have deeply influenced me and helped me to do better research.

Besides, I want to express my gratitude to Dr. Ioannis Schizas, Dr. Jean Gao, Dr. Saibun Tjuatja, Dr. Yan Wan for taking time to serve in my dissertation committee.

I am grateful to all the instructors who taught me valuable knowledge as I growing up. I also want to thank my colleagues and visiting scholars for their help and advice in our lab: Qiong Wu, Shitong Yuan, Na Wu, Hao Liang, Longwei Wang, Dheeral Bhole, Fangqi Zhu, Zikai Wang, Zhangliang Chen, Chengchen Mao, Supreet Huilgol, Dr. Liang Han, Dr. Zhuo Sun, Dr.Yupeng Li, Dr.Kuo Liao.

Last but not least, I would like to express my deep gratitude to my parents Limin Zhao and Lijuan Gan for their continuous support and encouragement during my graduate studies and their advices and helps through my toughest time.

This work was supported in part by U.S. Office of Naval Research (ONR) under Grant N00014-13-1-0043 and N00014-17-1-2733.

Nov 16, 2017

ABSTRACT

Massive MIMO Performance Analysis and Radar Sensor Networks-Based Target Detection

Ganlin Zhao, Ph.D.

The University of Texas at Arlington, 2017

Supervising Professor: Qilian Liang

In this dissertation, we apply massive multiple-input-multiple-output (MIMO) performance analysis and radar target detection based on radar sensor networks(RSN). In recent years, massive MIMO draws great interest for wireless communication researchers. As a highly scalable technology for 5G networks, massive MIMO will meet the increasing demand for wireless throughput. Also, radar target detection is also an important topic for military and civilian applications. Improving detection accuracy when target is embedded in strong background clutter is a challenging task.

In Chapter 2, we investigate scaling law of theoretical transmission capacity limit in an uplink multi-user MIMO system. In 5G network base station densification and massive MIMO are both important techlogogies which explore the spatial reuse and diversity to increase the total network spectrum efficiency. We apply scaling law to conduct the asymptotic analysis on how the outage capacity scales with number of users, base stations and base station antennas.

In Chapter 3, we investigate shadow fading impact on a multi-user massive MIMO system. By deploying a large antenna array on the base station, the random

channel vectors between users and base station antennas become pairwise orthogonal. This important property of massive MIMO makes small scale fading effect asymptotically vanish while large scale fading still remains. Based on this fact, we analyze the uplink achievable rate and cell coverage area under outage constraint considering log-normal shadow fading effect for both single-cell and multi-cell scenarios.

In Chapter 4, we propose an Empirical Mode Decomposition (EMD) based approach to Ultra Wide Band (UWB) radar for sense-through-foliage target detection. When the radar signal quality is good, the EMD based target detection approach performs well by comparing to the no target case. When the radar signal quality is poor and a single radar echo fails to detect the target, we firstly apply RSN and Rake structure to combine radar echoes from different radar cluster-members and then the EMD based method could successfully carry out the target detection.

In Chapter 5, we propose a target detection and classification approach using Hidden Markov Models (HMMs). Hidden Markov Model is used as an classifier to distinguish between the presence of target in a background clutter and the pure clutter response. Sense-through-foliage target detection and Sense-through-Wall human detection are conducted using real world Ultra Wide Band (UWB) data. Experiment results show HMM based method provides good detection and false alarm rate for poor quality radar echoes in position 1 in the sense-through-foliage target detection scenario. Sense-through-wall human experiment results shows Hidden Markov Model based method could successfully detect stationary human target behind different types of walls.

TABLE OF CONTENTS

LIST OF ILLUSTRATIONS

LIST OF TABLES

CHAPTER 1

Introduction

In the past few years, the fourth generation (4G) mobile communications systems have been deployed and used worldwide. With the explosive increasing number of wireless devices, the growing demand for higher data rate cannot be accommodated by 4G. Therefore, the fifth generation (5G) mobile communication systems, which are expected to be introduced by 2020, have attracted a great deal of research attention from both academia and industry.

As one of the most promising candidate technique for the 5G wireless network, massive MIMO or large-scale antenna systems has drawn significant research interests[1] [2] [3]. The concept of massive MIMO was first proposed in [3], where the asymptotic performance of noncooperative cellular systems was analyzed when the number of base station antennas is unlimited. It was shown in [3] that by employing simple linear signal processing, i.e., maximal ratio transmission (MRT) for the forward links and maximal ratio combining (MRC) for the reverse links, the effects of uncorrelated noise and small-scale fading are eliminated, and the transmit power can be made arbitrary small. In [4], the authors compared the two most prominent linear precoders, conjugate beamforming and zero-forcing (ZF), with respect to net spectral-efficiency and radiated energy-efficiency. In [5], the performance of multi-cellular MIMO systems was investigated when the number of base-station antennas was not extremely large compared to the number of users. The transmit power scaling laws and lower capacity bounds in the uplink massive MIMO systems were derived in [6], which showed that the power could be made inversely proportional to N in

the perfect channel state information (CSI) scenario and $\sqrt{N}$ in the imperfect CSI scenario, where N denotes the number of base station antennas. In [7], the authors investigated how massive MIMO performs in channels measured in real propagation environments and showed that the measured channels can achieve performance close to that in independent and identically distributed (i.i.d.) Rayleigh channels, so the theoretical advantages of massive MIMO can also be harvested in real channels.

Channel hardening effect as one important property occurs in massive MIMO channels, small scaling fading effect eventually average out. As the channel matrix H increases, the off-diagonal terms of the $H^H H$ matrix become increasingly less important compared to the diagonal terms. However, large scale fading effect still remains and the randomness in the large scale fading still has significant impact on system outage. The study on this impact of Massive MIMO is still open to date.

To meet 1000 traffic volume increment in 5G mobile communication systems, besides the technologies such as massive MIMO to improve the spectrum efficiency and millimeter wave communications to extend the transmission bandwidth, a larger number of small cells have to be densely deployed for 5G cellular networks. As a consequence, the base station densification is emerging as one of core characteristics for 5G cellular networks[8]. The capacity scaling law was firstly proposed to investigate large network performance with the scaling system parameters. To investigate the Massive MIMO performance in a densified network, scaling provides good asymptotic analysis insight.

Radar target detection is an important topic in both military and civilian research. Through foliage target detection plays and important role in modern warfare since the foliage environment provides good cover for military equipments such as tanks and artilleries. However, due to the non-stationary and impulsive nature

of foliage clutter the target detection task is not easy as in an stationary environment. Hilbert-Huang transformation (HHT) first proposed by N.E.Huang [9] is an algorithm mostly suited for non-linear and non-stationary signal analysis. The first phase of HHT is called empirical mode decomposition(EMD) which decomposes non-stationary signals as different mono-component oscillatory mode. Therefore, EMD may provide some insights considering the special characteristic of through foliage target detection task.

Hidden Markov Model (HMM) is a statistical model widely used in many pattern recognition problems. Radar target detection is essentially a binary classification task. To apply HMMs for radar target detection, HMMs represent target and clutter are trained. Testing radar signals are used to calculate likelihood under different pre-trained models and classified as the category (target or non-target) with higher likelihood.

CHAPTER 2

Uplink Outage Throughput Capacity Scaling Law of Massive MIMO Systems

2.1 Introduction

Massive MIMO technology appears as the result of increasing demand for wireless throughput. Current wireless broadband standard like long-term evolution (LTE) allows up to eight antennas at the base station. With more transmitting/receiving antennas equipped, more degrees of freedom can be obtained by the propagation channel either for multiplexing or diversity gain. In this case, Massive MIMO could break the limitation of number of equipped antennas on the base station side. Large antenna array with physically smaller antennas is installed on the base station. The magnitude of number of antennas could be more than one hundred. In [5], how much antennas would be sufficient for Massive MIMO is studied. Massive MIMO system is comprehensively studied in [6] and [10].

Throughput capacity is the key element to analyze the performance of networks. Channel capacity, indicates how much data could be reliably transmitted over communication channel, eventually depends on what channel model applies. For example, the capacity of AWGN channel is essentially different from fading channels. For AWGN channel, transmitter could send out data at a positive rate while having desired very small error probability. Fading channel can't guarantee to achieve this as long as the probability that channel in deep fading is non-zero. In slow fading scenario, outage capacity is always considered as it assumes that at a given rate R at which transmitter encodes data, whatever coding scheme used, the error probability cannot made be arbitrarily small. In other words, reliable communication occurs

when the random channel gain is strong enough to support the desired rate R. Otherwise, outage happens when capacity drops below R in deep fading situation. For fast fading scenario, channel cannot remain constant over symbol coherent period. Since codeword span over several coherent period, we can use block-fading model that consider several parallel sub-channels fade independently. The capacity can be assigned with positive value by coding over a large number of coherence time intervals in order to average independent fades of channels [11].

Capacity scaling law, firstly used in ad-hoc networks, is an asymptotic analysis method to investigate a large network performance with certain increasing system parameters, for example, the number of nodes, relays and infrustrutures.A lot of research works has been done. Gupta and Kumar [12] initiatively studied scaling law of a random ad-hoc wireless networks. When nodes are randomly placed in the network and they randomly choose a destination, the per-node capacity is shown to be $\Theta(\frac{W}{\sqrt{n \log n}})$ as the number of nodes n tends to infinity, where n is the number of nodes and W(the same below) is the transmitting rate each node is capable of using a fixed range. In [13], with b base stations and n nodes settings, the author proves that in order to achieve infrastructure gain, b should grow at least faster than $\sqrt{\frac{n}{\log n}}$ and the maximum throughput scales as $\Theta(bW)$ which increases linearly with the number of base stations. The scaling law of data transmission limit of hybrid wireless networks is studied in [14]. Squared cell model is assumed with b base stations and n wireless nodes and fading environment is considered. The per-node outage throughput capacity over Nakagami-m fading channel scales as $O\left(\log[\left(\epsilon^{\frac{1}{m}}\right)^{\frac{b}{n}} \frac{n}{b}]W_1\right)$ under ad-hoc mode and $\Theta\left(\frac{b}{n}\log\left(\epsilon^{\frac{1}{m}}\frac{n}{b}\right)W_2\right)$ under infrastructure mode, where W_1 is the bandwidth shared by ad-hoc transmission and uplink infrastructure transmission and W_2 is bandwidth assigned for downlink infrastructure transmission.

With the tremendous growing number of mobile users in the next generation wireless networks, the base station densification[8] is proposed by implementing more base stations to reuse the time frequency resources which could benefit the whole network throughput. Massive MIMO technology also explores the spatial diversity to increase the spectrum efficiency. Therefore, applying capacity scaling law to study the system with increasing number of users, base stations and number of antennas is an intrinsically useful. In this paper, we focus on studying how the uplink outage capacity scales with number of base stations b, number of users n, as well as large number of antennas M on the base station and we derive the outage capacity in closed-form expression.

2.2 Network Modeling

The following network model is considered throughout this chapter:

1. The network consists of n users and b base stations.
2. The whole network is considered as in a unit circle area and evenly divided into b circular cells with cell radius c. We assume gaps between cells can be neglected so all cells occupies the whole area.
3. Each cell contains only one base station in the center. There exists K users uniformly distributed along the cell radius in each cell. The user distance to base station is denoted as $r_k \in [c_0, c]$, where c_0 denotes the radius of an exclusive region around base station.
4. We assume all base stations are wired interconnected to form an infrastructure with unlimited bandwidth. Base stations neither consume nor generate data and they only serve as traffic relays compared to nodes.
5. For the purpose of studying the scaling law of number of base stations and users in the network, $b = O(\frac{n}{\log n})$ is assumed that b increases at a slower rate than

n. Study [13] shows that in a probabilistic routing strategy, a node chooses between infrastructure and ad-hoc mode according to some probability. For example, if b grows slower than $\sqrt{\frac{n}{\log n}}$, the maximum throughput capacity behaves asymptotically same as pure ad-hoc networks which means no real benefit for using infrastructure. If b grows faster than $\sqrt{\frac{n}{\log n}}$, maximum capacity increases linearly with number of base stations b. Therefore, investment on base station should be at least $\sqrt{\frac{n}{\log n}}$ to achieve infrastructure capacity gain. In this case, our assumption should be enough to have infrastructure gain.

6. Multi-user MIMO is preferred in this work compared to Point-to-Point MIMO for its significant simplification of the terminal device. Each user terminal is assumed to have only one antenna.
7. The base station located in each cell has an array of M antennas. The antennas are sufficient to simultaneously serve all K users in the cell. The number of antennas greatly exceeds the number of terminals $M \gg K$.
8. In uplink transmission, the following model are assumed per channel use[10]:

$$\mathbf{x}_u = \sqrt{\rho}_u \mathbf{G}\mathbf{q}_u + \mathbf{w}_u \tag{2.1}$$

Where $\mathbf{q}_u$ is a $K \times 1$ vector cosists of QAM symbols transmitted by K users, $\mathbf{x}_u$ is the antenna array received vector of size $M \times 1$. $\mathbf{w}_u$ is a $M \times 1$ vector of received noise whose entries are independent and identical distributed (i.i.d.) complex Gaussian random variables with zero mean and unit variance. ρ_u is proportional to SNR. Each terminal is constrained to have an expected power of one,

$$E\{|q_{uk}|^2\} = 1, k = 1, ..., K.$$

$\mathbf{G}$ is $M \times K$ propagation channel matrix, which is composed of small-scale fading and large scale fading factors:

$$\mathbf{G} = \mathbf{H}\mathbf{D}_{\beta}^{1/2} \tag{2.2}$$

In the equation above, Matrix $\mathbf{H}$ accounts for small-scale fading whose dimension is $M \times K$. Each entry is the complex small-scale fading coefficient (for example, fading coefficient follows Rayleigh or Rician distribution) between the Kth user terminal and the Mth antenna on base station. Matrix $\mathbf{D}_{\beta}^{1/2}$ is a $K \times K$ diagonal matrix. The diagonal entries of $\mathbf{D}_{\beta}^{1/2}$ are normalized large-scale fading coefficients related to the antenna array and Kth user terminal.

2.3 Preliminaries

2.3.1 The Number of Nodes Per Cell

As number of base stations $b = O(\frac{n}{\log n})$ and number of users $n \to \infty$, there exists $K = \Theta(\frac{n}{b})$ nodes within each cell. The cell radius is bounded by $c = O(\frac{1}{b})$.

Proof: Let event A denote a Bernoulli event that a particular node i, $1 \leq i \leq n$, will fall into a particular cell of area πc^2. Because nodes are uniformly distributed in the network, it is clear that probability of event A is $P_A = \frac{n/b}{n} = \frac{1}{b}$. Therefore, the number of nodes, K, has a binomial distribution with parameters (P_A, n). Using Chernoff bound, we have

$$Pr(K > k_1 \frac{n}{b}) \leq \frac{E\{\exp(K)\}}{\exp(\frac{k_1 n}{b})}$$

where k_1 is a constant. Since $E\{\exp(K)\} = (1+(e-1)P_A)^n \leq \exp[(e-1)\frac{n}{b}]$ (because $1 + x \leq exp(x)$), we arrive at

$$Pr(K > k_1 \frac{n}{b}) \leq \exp\left\{ -\frac{n}{b}[k_1 - (e-1)] \right\}.$$

As long as $k_1 > e-1$, we know by the union bound that Pr(some cells have more than $\frac{k_1 n}{b}$ nodes) converges to zero as n tends to infinity.

Similarly,

$$Pr(K < k_2 \frac{n}{b}) \leq \frac{E\{\exp(-K)\}}{\exp(\frac{-k_2 n}{b})}$$

where k_2 is also a constant. Since $E\{\exp(-K)\} = (1+(e^{-1}-1)P_A)^n \leq \exp[(e^{-1}-1)\frac{n}{b}]$, we obtain

$$Pr(K < k_2 \frac{n}{b}) \leq \exp\left\{ -\frac{n}{b}[(1-e^{-1}) - k_2] \right\}.$$

As long as $k_2 < 1 - e^{-1}$, we know by the union bound that Pr(some cells have less than $\frac{k_2 n}{b}$ nodes) converges to zero as n tends to infinity. Hence, it is concluded that each cell contains $\Theta(\frac{n}{b})$ nodes and we complete the proof.

2.3.2 Fenton-Wilkinson Method

The summation of several independent log-normal random variables can be approximated by another log-normal random variable with appropriately chosen parameters[15],

$$I = \sum_{k=1}^{N_I} 10^{\Omega_{k(dBm)}/10} \approx 10^{Z_{(dBm)}/10} = \hat{I} \tag{2.3}$$

where $\Omega_{k(dBm)}$ are Gaussian random variables with means $\mu_{\Omega_{k(dBm)}}$ and variances $\sigma^2_{\Omega_k}$, $Z_{(dBm)}$ is a Gaussian random variable with mean $\mu_{Z_{(dBm)}}$ and variance σ^2_Z, so that,

$$\Omega_k = 10^{\Omega_{k(dBm)}/10}$$

$$Z = 10^{Z_{dBm}/10}$$

where Ω_k and Z are the log-normal random variables. The problem is to determine $\mu_{Z_{(dBm)}}$ and σ^2_Z in terms of $\mu_{\Omega_{k(dBm)}}$ and $\sigma^2_{\Omega_k}$.

The mean $\mu_{Z_{(dBm)}}$ and variance σ^2_Z can be obtained by matching the first two moments of the approximation $\hat{I}$. For space limitation, we omit the proof of the derivation.

$$\mu_{\hat{Z}} = \frac{\sigma_{\hat{\Omega}}^2 - \sigma_{\hat{Z}}^2}{2} + \ln\left(\sum_{k=1}^{N_I} e^{\mu_{\hat{\Omega}_k}}\right) \tag{2.4}$$

$$\sigma_{\hat{Z}}^2 = \ln\left(\left(e^{\sigma_{\hat{\Omega}}^2} - 1\right)\frac{\sum_{k=1}^{N_I} e^{2\mu_{\hat{\Omega}_k}}}{\left(\sum_{k=1}^{N_I} e^{\mu_{\hat{\Omega}_k}}\right)^2} + 1\right) \tag{2.5}$$

Note that nature logarithms are used here for convenient purpose.

$$\Omega_k = 10^{\Omega_{k(dBm)}/10} = e^{\xi\Omega_{k(dBm)}} = e^{\hat{\Omega}_k}$$

where $\xi = (\ln 10)/10 = 0.23026$ and $\hat{\Omega}_k = \xi\Omega_{k(dBm)}$. Also $\mu_{\hat{\Omega}_k} = \xi\mu_{\Omega_{k(dBm)}}$ and $\sigma_{\hat{\Omega}_k}^2 = \xi^2\sigma_{\Omega_k}^2$. The same applies to Z where $\hat{Z} = \xi Z_{(dBm)}$. Since standard deviation of log-normal shadowing is largely independent of the radio path length, identical variances are often assumed that for $\hat{\Omega}_k, k = 1, ..., N_I$, $\sigma_{\hat{\Omega}_k}^2 = \sigma_{\hat{\Omega}}^2$. Finally,

$$\mu_{Z_{(dBm)}} = \xi^{-1}\mu_{\hat{Z}} \tag{2.6}$$

$$\sigma_Z^2 = \xi^{-2}\sigma_{\hat{Z}}^2 \tag{2.7}$$

2.4 Scaling Law of Uplink Outage Throughput Capacity

In this section, we focus on investigation of uplink Massive MIMO performance in terms of outage capacity. With very large antenna array on the base station, a lot of things become different from the traditional MIMO system point of view.

One of the key characters that base station antennas greatly exceeds the number of user terminals is called favorable propagation[16]. The vector value based propagation matrix are asymptotically orthogonal as $M \gg K$. The propagation matrix $\mathbf{G}$ is described in equation (2.2) which contains both small scale fading matrix $\mathbf{H}$ and large scale fading diagonal matrix $\mathbf{D}_\beta^{1/2}$. Each column-vector of $\mathbf{H}$ correlates to small scale fading between the kth terminal and the M base station antennas. When

$M \gg K$, column-vectors in matrix $\mathbf{H}$ become long and are asymptotically pairwise orthogonal according to random matrix theory[5]. The propagation matrix thus can be written as:

$$\left(\frac{\mathbf{G}^H\mathbf{G}}{M}\right)_{M\gg K} = \mathbf{D}_\beta^{1/2}\left(\frac{\mathbf{H}^H\mathbf{H}}{M}\right)_{M\gg K}\mathbf{D}_\beta^{1/2} \approx \mathbf{D}_\beta \tag{2.8}$$

From equation (2.8) we can observe that long propagation matrix makes small scale fading effect greatly mitigated under favorable propagation while large scale fading coefficient dominates.

The sum rate capacity of uplink MU-MIMO can be obtained [11] assuming base station has perfect instantaneous channel state information:

$$C_{sum\_ul} = \log_2 \det\left(\mathbf{I}_K + \rho_u \mathbf{G}^H\mathbf{G}\right) \tag{2.9}$$

by applying favorable propagation $\left(\mathbf{G}^H\mathbf{G}\right)_{M\gg K} \approx M\mathbf{D}_\beta$, we get

$$C_{sum\_ulM\gg K} \approx \log_2 \det\left(\mathbf{I}_K + M\rho_u \mathbf{D}_\beta\right) \tag{2.10}$$

$\mathbf{D}_\beta$ is a diagonal matrix that $\mathbf{D}_\beta = diag\{\beta_1, \beta_2, ..., \beta_K\}$, equation (11) can be rewritten as:

$$C_{sum\_ulM\gg K} = \sum_{k=1}^{K} \log_2\left(1 + M\rho_u\beta_k\right) \tag{2.11}$$

Equation (12) indicates that the sum-rate could be represented as individual rate correlated to each terminal. This yields an simplification of linear decoding process by using matched-filter at the BS.

We already observe that large-scale fading is a dominant factor in capacity equation. To further derive the outage capacity of the uplink channel, we assume each large-scale fading coefficient β_k has the following expression[17]:

$$\beta_k = \phi r_k^{-\alpha}\zeta_k \tag{2.12}$$

Where ϕ is a constant related to the antenna gain and carrier frequency, r_k is the distance between the base station and kth terminal. α is the path loss exponent. ζ_k is the log-normal shadowing with $10\log_{10}\zeta_k \sim \mathcal{N}(0,\sigma_k^2)$. Thus we apply this path loss and shadowing model to equation (12),

$$C_{sum\_ulM\gg K} = \sum_{k=1}^{K} \log_2\left(1 + M\rho_u\phi d_k^{-\alpha}\zeta_k\right) \tag{2.13}$$

We assume that all user terminal devices transmit at a sum rate $R\ bit/s/Hz$, the related outage probability is

$$P_{out} = Pr\left\{\sum_{k=1}^{K} \log_2\left(1 + M\rho_u\phi d_k^{-\alpha}\zeta_k\right) < R\right\} \tag{2.14}$$

To solve the equation above, we then explore the outage capacity both in high SNR and low SNR scenarios.

2.4.1 Low SNR

At low SNR, we employing $\ln(1+x) \approx x$ and obtain the following,

$$P_{out} = Pr\left\{\log_2^e M\rho_u\phi \sum_{k=1}^{K}\left(d_k^{-\alpha}\zeta_k\right) < R\right\} \tag{2.15}$$

Since ζ_k is log-normal distributed with $10\log_{10}\zeta_k \sim \mathcal{N}(0,\sigma_k^2)$, we could derive $d_k^{-\alpha}\zeta_k$ is also log-normal distributed with $10\log_{10}\left(d_k^{-\alpha}\zeta_k\right) \sim \mathcal{N}(\mu_k,\sigma_k^2)$ where $\mu_k = 10\log d_k^{-\alpha}$.

We assume users in the cell suffers independent shadow fading. Applying Fenton-Wilkinson method we approximate the summation of log-normal distributed random variables $d_k^{-\alpha}\zeta_k$ with a new log-normal random variable, say χ that $10\log_{10}\chi \sim \mathcal{N}(\mu_\chi,\sigma_\chi^2)$. The new parameter of χ is chosen by,

$$\mu_\chi = \xi^{-1}\left(\frac{\xi^2}{2}\left(\sigma_k^2 - \sigma_\chi^2\right) + \ln\left(\sum_{k=1}^{K} r_k^{-\alpha}\right)\right) \tag{2.16}$$

$$\sigma_\chi^2 = \xi^{-2} \ln \left(\left(e^{\xi^2 \sigma_k^2} - 1 \right) \frac{\sum_{k=1}^{K} r_k^{-2\alpha}}{\left(\sum_{k=1}^{K} r_k^{-\alpha} \right)^2} + 1 \right) \tag{2.17}$$

Then the outage probability is,

$$\begin{aligned} P_{out} &= Pr\left\{ \log_2^e M \rho_u \phi \chi < R \right\} \\ &= Pr\left\{ \chi < \frac{R}{\log_2^e M \rho_u \phi} \right\} \end{aligned} \tag{2.18}$$

The cumulative distribution function(CDF) of the log-normal distributed random variable χ is given by

$$F(x) = \frac{1}{2} erfc\left(-\frac{\ln x - \mu_\chi}{\sigma_\chi \sqrt{2}} \right) \tag{2.19}$$

where $erfc(x)$ is the complementary error function.

With the CDF of χ, we have the following

$$\begin{aligned} P_{out} &= F(T) \\ &= \frac{1}{2} erfc\left(-\frac{\ln T - \mu_\chi}{\sigma_\chi \sqrt{2}} \right), T = \frac{R}{\log_2^e M \rho_u \phi} \end{aligned} \tag{2.20}$$

Unfortunately there's no closed form expression of $erfc(x)$ in terms of elementary functions. According to [18], an tight exponential upper bounds and a pure exponential approximation for the complementary error function are derived

$$erfc(x) \leq \frac{1}{2} e^{-2x^2} + \frac{1}{2} e^{-x^2} \leq e^{-x^2}, x > 0 \tag{2.21}$$

$$erfc(x) \approx \frac{1}{6} e^{-x^2} + \frac{1}{2} e^{-\frac{4}{3} x^2}, x > 0 \tag{2.22}$$

Applying the approximation of equation(2.21), we got

$$P_{out} = \frac{1}{2} \left(\frac{1}{6} T' + \frac{1}{2} \left(T' \right)^{\frac{4}{3}} \right), \tag{2.23}$$

where

$$T' = e^{-\left(-\frac{\ln T - \mu_\chi}{\sigma_\chi \sqrt{2}} \right)^2} \tag{2.24}$$

The outage capacity is obtained by solving $P_{out} = \epsilon$. However, solving the non-linear equation by applying newton's method does not turn out to obtain physically meaningful root. Therefore, we try to approximate the complementary error function using the tight upper bound (2.21) to get a linear equation.

$$P_{out} \leq \frac{1}{2}\left(\frac{1}{2}\left(T'\right)^2 + \frac{1}{2}T'\right) = \epsilon \tag{2.25}$$

where

$$T' = \frac{\sqrt{1+16\epsilon}-1}{2} \tag{2.26}$$

Equation (2.26) is satisfied when $\epsilon < \frac{1}{2}$ Combining (2.24) and (2.26) we got

$$C_\epsilon = \log_2^e M\rho_u\phi exp\left\{\mu_\chi - \sigma_\chi\sqrt{2\ln\left(\frac{2}{\sqrt{1+16\epsilon}-1}\right)}\right\} \tag{2.27}$$

From equation (2.27) we can see that the capacity is related to μ_χ and σ_χ which are defined in (2.16) and (2.17).

With uniform distributed users in each cell, the distance r_k between the kth user in one cell and the base station has the following probability density function:

$$f_{r_k,\theta}(r_k,\theta) = \begin{cases} \frac{r_k}{\pi c^2}, & 0 \leqslant r_k \leqslant c, 0 \leqslant \theta \leqslant 2\pi \\ 0, & otherwise \end{cases}$$

By applying the weak law of large numbers to the summation term of the numerator and denominator in equation (2.17) we are able to obtain the following:

$$\begin{aligned} \sum_{k=1}^{K} r_k^{-2\alpha} &= KE\left\{r_k^{-2\alpha}\right\} \\ &= K\int_{c_0}^{c}\int_{2\pi}^{0}\frac{r_k^{1-\alpha}}{\pi c^2}dr_k d\theta \\ &= \frac{K(c_0^{2(1-\alpha)} - c^{2(1-\alpha)})}{c^2(\alpha-1)}, \end{aligned}$$

and

$$\left(\sum_{k=1}^{K} r_k^{-\alpha}\right)^2 = K^2 E^2\left\{r_k^{-\alpha}\right\} = \frac{4K^2(c_0^{2-\alpha} - c^{2-\alpha})^2}{c^4(\alpha-2)^2}.$$

Then equation (2.18) can be rewritten as:

$$\sigma_\chi^2 = \xi^{-2}\ln\left(\left(e^{\xi^2\sigma_k^2} - 1\right)\frac{c^2}{4K(\alpha-1)c_0^2} + 1\right). \tag{2.28}$$

Based on the number of users K is bounded by $\Theta(\frac{n}{b})$ and cell radius c is bounded by $O(\sqrt{\frac{1}{b}})$ as the number of base stations increases, after some arithmetic manipulations by dropping the terms in equation(2.28) which are not scaling with n and b, we can obtain that $\sigma_\chi^2 = O(\log\frac{1}{n})$. Also, apply the same procedure to equation(2.17) we can obtain that $\mu_\chi = O(\log n)$.

Then based on equation(2.28) we make the conclusion that the transmission rate under low SNR for Massive MIMO uplink is:

$$R_{ul}^{low} = O\left(Mne^{-\sqrt{\log\left(\frac{1}{n}\right)\delta_\epsilon}}\right) \quad bit/s/Hz \tag{2.29}$$

Where $\delta_\epsilon = 2\ln\left(\frac{2}{\sqrt{1+16\epsilon}-1}\right)$.

From equation (2.29) we can see that in low SNR scenario, uplink outage capacity scales linearly with number of base stations M, which means that increasing number of antennas will always be helpful. We also observed that the outage capacity has no relation with number of base stations b in this case. Fig.2.1 shows uplink outage capacity with different M settings when outage probability $\epsilon = 0.001$.

2.4.2 High SNR

In high SNR scenario, we approximate $\log(1+x) = \log(x)$ to equation (2.14),

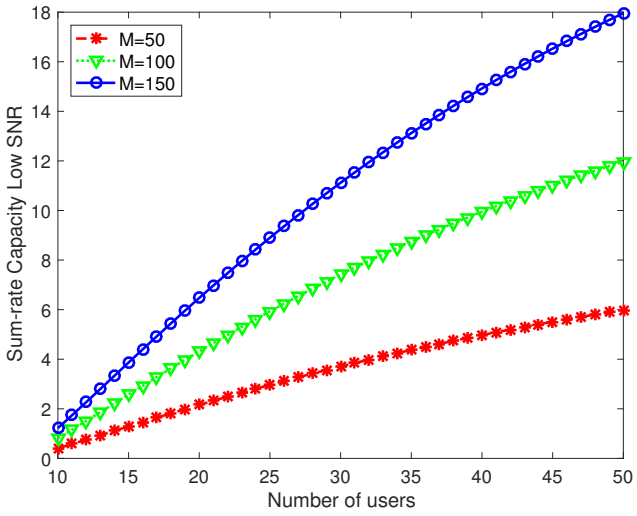

Figure 2.1. Uplink outage throughput capacity under low SNR scenario ($\epsilon = 0.001$).

$$P_{out} = Pr\left\{\sum_{k=1}^{K} \log_2\left(M\rho_u\phi d_k^{-\alpha}\zeta_k\right) < R\right\} \tag{2.30}$$

From the previous section we have seen that ζ_k is log-normal distributed with $10\log_{10}(\zeta_k) \sim \mathcal{N}(0, \sigma_k^2)$. We define another random variable $L = \log_2 M\rho_u\phi d_k^{-\alpha}\zeta_k$ that $L \sim \mathcal{N}(\mu_L, \sigma_L^2)$ and

$$\mu_L = \log_2(M\rho_u\phi d_k^{-\alpha}) \tag{2.31}$$

$$\sigma_L^2 = (\frac{\sigma_k}{10\log_{10} 2})^2 \tag{2.32}$$

The summation of independent normal distributed random variables is also normal distributed. We denote the summation as $\hat{L} = \sum_{k=1}^{K} L$, $\hat{L} \sim \mathcal{N}(\mu_{\hat{L}}, \sigma_{\hat{L}^2})$. Based on

the assumption that users are uniform distributed within each cell and apply the law of large numbers we can obtain the mean $\mu_{\hat{L}}$ as

$$\begin{aligned}
\mu_{\hat{L}} &= \sum_{k=1}^{K} \log_2(M\rho_u\phi r_k^{-\alpha}) \\
&= KE\left\{\log_2(M\rho_u\phi r_k^{-\alpha})\right\} \\
&= K\int_{c_0}^{c}\int_{2\pi}^{0} \log_2(M\rho_u\phi r_k^{-\alpha})\frac{r_k}{\pi c^2}dr_k d\theta \\
&= \frac{K}{2c^2}\log_2^e[(c^2-c_0^2)(2\ln M\rho_u\phi+\alpha)-2\alpha(c^2\ln c - c_0^2\ln c_0)], \qquad (2.33)
\end{aligned}$$

and

$$\begin{aligned}
\sigma_{\hat{L}}^2 &= K\sigma_L^2. \\
&= K(\frac{\sigma_k}{10\log_{10}2})^2. \qquad (2.34)
\end{aligned}$$

Then we can rewrite equation (3.30)

$$\begin{aligned}
P_{out} &= Pr\left\{\sum_{k=1}^{K} L < R\right\} \\
&= Pr\left\{\hat{L} < R\right\} \\
&= \frac{1}{2}erfc\left(-\frac{R-\mu_{\hat{L}}}{\sigma_{\hat{L}}\sqrt{2}}\right) = \epsilon \qquad (2.35)
\end{aligned}$$

Apply approximation (2.21)

$$C_\epsilon = \mu_{\hat{L}} - \sigma_{\hat{L}}\sqrt{2\ln\left(\frac{2}{\sqrt{1+16\epsilon}-1}\right)}, \epsilon < \frac{1}{2} \qquad (2.36)$$

Applying the scaling law to (2.34) and (2.35), we can get $\mu_{\hat{L}} = O(\frac{n}{b}\log(Mb))$ and $\sigma_{\hat{L}} = O(\sqrt{\frac{n}{b}})$ So the transmission rate under high SNR for Massive MIMO uplink is:

$$R_{ul}^{high} = O\left(\frac{n}{b}\log(Mb) - \sqrt{\frac{n}{b}\delta_\epsilon}\right) \quad bit/s/Hz \qquad (2.37)$$

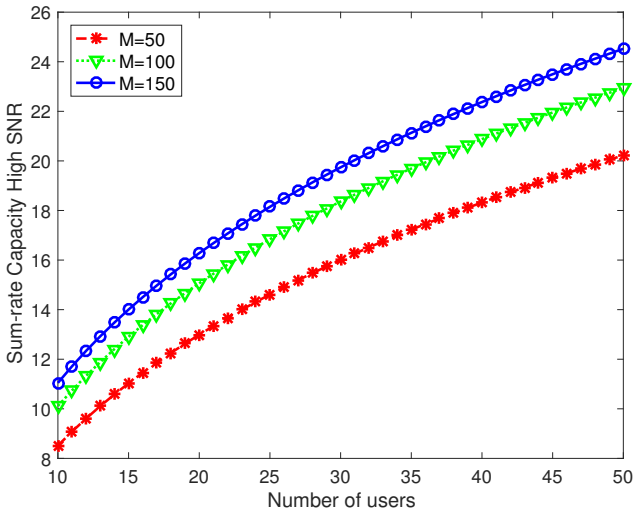

Figure 2.2. Uplink outage throughput capacity under high SNR scenario ($\epsilon = 0.001$).

Where $\delta_\epsilon = 2\ln\left(\frac{2}{\sqrt{1+16\epsilon}-1}\right)$.

Under high SNR scenario, the uplink outage throughput capacity yields logarithmic increase with number of base station antennas M. From Figure 2.2 we can see that increasing M from 50 to 100 only has half capacity gain when increasing M from 25 to 50, which means that at high SNR we are getting less benefit from adding more antennas.

2.5 Conclusions

In this chapter, we derived the theoretical uplink outage throughput capacity of a multi-user Massive MIMO system. Under favorable propagation condition, small scale fading is averaged out according to asymptotic orthogonality of the propagation matrix with increased base station antenna M. Large scale fading on throughput capacity is examined for both high SNR and low SNR case. Close-form outage throughput capacity is derived. We proved that at low SNR, the infrastructure mode uplink

outage capacity is $O\left(Mne^{-\sqrt{\log\left(\frac{1}{n}\right)\delta_\epsilon}}\right)$ $bit/s/Hz$. At high SNR, the infrastructure uplink outage capacity is $O\left(\frac{n}{b}\log(Mb) - \sqrt{\frac{n}{b}\delta_\epsilon}\right)$ $bit/s/Hz$. Increasing number of antennas at low SNR scenario yields better capacity gain compared to high SNR case.

CHAPTER 3

Outage Analysis of Uplink Massive MIMO System

3.1 Introduction

Massive MIMO firstly proposed in[3], serves as a key technology to meet the fast growth of data demand of 5G networks. MIMO technology could bring more degree of freedom of the propagation channel in terms of multiplexing gain or diversity gain. As a break through of long-term evolution(LTE) standard which allows at most eight antennas on the base station, massive MIMO deploys hundreds of base station antennas simultaneously serve tens of users[10]. Traditionally, for multiple collocated antenna placement, a minimum separation of half wavelength between any two antennas are required in order to mitigate the coupling effect. With a large number of antennas, the antenna array could occupy much larger area on the base station. In millimeter wave communications, with above 30GHz spectrum and shorter wavelength. antennas can be placed closer to each other which facilitates massive MIMO implementation.

As a promising technology for the upcoming 5G networks, massive MIMO has drawn intensive research interests[3][5][6][10]. In [3], as number of basestation antennas goes large, linear precoding and decoding are shown to be optimal and intra-cell interference and uncorrelated noise disappears. In [5], the performance of multi-cell MIMO system is studied with a large but finite number of antennas. In [19], the optimal number of users are investigated considering pilot allocation. In [6], spectral and energy efficiency of uplink massive MIMO system are compared under different detection methods, tradeoff between energy and spectral efficiency are also studied.

As a result, uplink transmit power could be made arbitrarily small which is significant for saving user terminal battery life. Further, with a large number of antennas, the channel vectors between users and base station are very long and pairwise orthogonal. This effect averages out small scale fading by using simple linear signal processing method [3]. However, the large scale fading still remains. The large scale fading essentially contains random variation of shadow fading imposed on the distant-dependent path loss. Shadow fading is mainly caused by obstructions and other propagation effects. Especially in urban area, buildings and other blockages result in higher shadow fading than open area.

It is important for engineers to statistically model shadow fading for system design. Based on this fact, question about how the randomness in shadow fading could effect massive MIMO performance arise. In [20], large scale fading effect of massive MIMO are analyzed under gamma distributed shadow fading and the average asymptotic ergodic rate are derived considering both perfect CSI and imperfect CSI. To tackle with this problem from the outage perspective, we assume log-normal distributed shadow fading and make analysis based on the asymptotic achievable rate for a given outage probability. Next, we use cell coverage area as another metric to evaluate the average cell performance.

3.2 System Model

In this work, we consider an uplink multiuser massive MIMO system. The base station located in a cell has an array of M antennas simultaneously serves K single antenna user terminals. The number of base station antennas greatly exceeds the number of terminals $M \gg K$. In uplink transmission, the $M \times 1$ received signal vector at the base station is:

$$\mathbf{y} = \sqrt{\rho}\mathbf{G}\mathbf{x} + \mathbf{w} \tag{3.1}$$

Where $\mathbf{x}$ is a $K \times 1$ signal vector transmitted by K users. $\mathbf{w}$ is a $M \times 1$ vector of received noise whose entries are i.i.d. complex Gaussian random variables with zero mean and unit variance. ρ is a measure of transmit signal-to-noise ratio. $\mathbf{G}$ is the $M \times K$ propagation channel matrix between users and base station, which is composed of small-scale fading and large scale fading factors:

$$\mathbf{G} = \mathbf{H}\mathbf{D}^{1/2} \tag{3.2}$$

In the equation above, Matrix $\mathbf{H}$ accounts for small-scale fading whose dimension is $M \times K$. Each element of $\mathbf{H}$ is zero mean i.i.d small-scale fading coefficient between the kth user terminal and the mth antenna on base station. Matrix $\mathbf{D}^{1/2}$ is a $K \times K$ diagonal matrix whose elements are large-scale fading coefficients $\beta_k^{1/2}$ of the kth user terminal to the base station.

In this work, we model the large scale fading coefficient as follows[17]:

$$\beta_k = \phi r_k^{-\alpha} \zeta_k \tag{3.3}$$

Where ϕ is a constant related to the antenna gain and carrier frequency, r_k is the distance between the base station and kth terminal. α is the path loss exponent. ζ_k is the log-normal shadowing with $\zeta_k \sim 10\log_{10}\mathcal{N}(0, \sigma_k^2)$. The probability density function of lognormal random variable is:

$$f(x) = \frac{10\log e}{\sigma\sqrt{2\pi}x} e^{-\frac{(10\log x - \mu)^2}{2\sigma^2}} \tag{3.4}$$

We also assume disk shape cell with radius c that users in each cell are uniformly distributed and base station is at the cell center. The distance distribution from user to cell center is:

$$f_{r,\theta}(r,\theta) = \begin{cases} \frac{r}{\pi c^2}, & 0 \leqslant r \leqslant c, 0 \leqslant \theta \leqslant 2\pi \\ 0, & otherwise \end{cases}$$

3.3 Single-Cell Uplink Outage Analysis

In this section, we study the performance of uplink massive MIMO system of single cell case. Both perfect CSI and imperfect CSI are evaluated.

3.3.1 Perfect CSI

With perfect CSI assumption, the base station knows channel matrix $\mathbf{G}$. We assume base station applies MRC detection. The received signal in (3.1) at the base station can be separated by multiplying $\mathbf{G}^H$, we can obtain:

$$\begin{aligned} \mathbf{r} &= \mathbf{G}^H\mathbf{y} \\ &= \sqrt{\rho}\mathbf{G}^H\mathbf{G}\mathbf{x} + \mathbf{G}^H\mathbf{w} \end{aligned} \tag{3.5}$$

The propagation matrix $\mathbf{G}$ described in equation (3.2) contains both small scale fading matrix $\mathbf{H}$ and large scale fading diagonal matrix $\mathbf{D}^{1/2}$. We denote $\mathbf{h}_k$ as the kth column-vector of $\mathbf{H}$. When the number of antennas M is large and $M \gg K$, the column vectors $\mathbf{h}_1, \mathbf{h}_2, ..., \mathbf{h}_k$ becomes long and pairwise orthogonal according to random matrix theory. For rayleigh fading, the following results are obtained based on [16]:

$$\begin{aligned} &\frac{1}{M}||\mathbf{h}_k||^2 \xrightarrow{\text{a.s.}} E\{|h_{ik}|^2\} = 1 \\ &\frac{1}{M}\mathbf{h}_k^H\mathbf{h}_i \xrightarrow{\text{a.s.}} 0, k \neq i \end{aligned} \tag{3.6}$$

where $\xrightarrow{\text{a.s.}}$ denotes almost sure convergence. Based on (3.6) we have,

$$\mathbf{G}^H\mathbf{G} = \mathbf{D}^{1/2}\mathbf{H}^H\mathbf{H}\mathbf{D}^{1/2} \approx M\mathbf{D} \tag{3.7}$$

The received signal at base station can be simplified as,

$$\mathbf{r} \approx \sqrt{\rho} M \mathbf{D} \mathbf{x} + \mathbf{G}^H \mathbf{w} \tag{3.8}$$

From (3.8) we can observe that each user can get a SNR of $M\rho\beta_k$. Therefore, the asymptotic achievable rate of the kth user is

$$\begin{aligned} R_k^P &= \log_2(1 + M\rho\beta_k) \\ &= \log_2(1 + M\rho\phi r_k^{-\alpha}\zeta_k) \end{aligned} \tag{3.9}$$

Due to the asymptotic orthogonality of channel matrix with large M, the maximum achievable rate of each user does not include small scale fading while large scale fading still exists. Conditioned on user location, suppose each user encodes data at the rate of R, then the system is said to be in outage if $R_k^P < R$[11]. The related outage probability is

$$P_{out} = Pr\{\log_2(1 + M\rho\phi r_k^{-\alpha}\zeta_k) < R\} \tag{3.10}$$

$$= Pr\{\zeta_k < \frac{2^R - 1}{M\rho\phi r_k^{-\alpha}}\} \tag{3.11}$$

Since ζ_k is a log-normal random variable represents shadow fading that $10\log_{10}\zeta_k \sim \mathcal{N}(0, \sigma_k^2)$, we can rewrite equation(3.11) as

$$P_{out} = 1 - Q\left(\frac{10\log\frac{2^R-1}{M\rho\phi r_k^{-\alpha}}}{\sigma_k}\right) \tag{3.12}$$

Where $Q(\cdot)$ is the Q-function.

We define the maximum achievable rate $R_{k,\epsilon}^P$ of the kth user as the outage probability P_{out} is less than a given threshold ϵ[14]. By solving $P_{out} = \epsilon$, $R_{k,\epsilon}^P$ can be expressed as

$$R_{k,\epsilon}^P = log_2(1 + M\rho\phi r_k^{-\alpha} 10^{0.1\sigma_k Q^{-1}(1-\epsilon)}) \tag{3.13}$$

Another metric could be used to evaluate the average cell performance under a given outage constraint is the cell coverage area[21]. For uplink transmission with a given minimum SNR requirement p_m, if the received signal power at the base station for a given user exceeds p_m, we say the user at this location is in the coverage area. Note that the outage probability P_{out} from (3.12) is derived under the rate constraint $R_k^P < R$. We now denote P_{cov} as the probability that the received power at the base station for a user satisfies the minimum SNR requirement:

$$\begin{aligned} P_{cov} &= Pr\{SNR_k > p_m\} \\ &= Pr\{M\rho\phi r_k^{-\alpha}\zeta_k > p_m\} \\ &= Pr\{\zeta_k > \frac{p_m}{M\rho\phi r_k^{-\alpha}}\} \\ &= Q\left(\frac{10\log\frac{p_m}{M\rho\phi r_k^{-\alpha}}}{\sigma_k}\right) \end{aligned} \tag{3.14}$$

According to [21], the cell coverage area is defined as the average percentage of locations where the users at these locations satisfied the minimum SNR requirement. Considering users are uniformly distributed within the cell, the probability of cell coverage area with cell radius c can be calculated as

$$\begin{aligned} C^P &= \int_0^{2\pi}\int_0^c P_{cov}\frac{r}{\pi c^2}drd\theta \\ &= \frac{2}{c^2}\int_0^c Q\left(\frac{10\log\frac{p_m}{M\rho\phi r_k^{-\alpha}}}{\sigma_k}\right)rdrd\theta. \end{aligned} \tag{3.15}$$

Calculating the integral in (3.15) yields

$$C^P = Q(A) + exp[2(\frac{1-AB}{B^2})]Q(\frac{2}{B} - A), \tag{3.16}$$

where

$$A = \frac{10\log\frac{p_m c^\alpha}{M\rho\phi}}{\sigma_k}, B = \frac{10\alpha\log e}{\sigma_k}. \tag{3.17}$$

3.3.2 Imperfect CSI

Practically, base station needs to estimate the channel matrix $\mathbf{G}$ by using uplink pilots send from user terminals. During the uplink coherent interval, each user transmit τ pilot symbols where $\tau \geq K$. Therefore, we denote $K \times \tau$ matrix $\mathbf{\Psi}$ as transmitted pilot matrix that the kth row vector of $\mathbf{\Psi}$ corresponds to the pilot sequence assigned for the kth user. Assuming pilot sequences sent by users are orthogonal we have $\mathbf{\Psi}\mathbf{\Psi}^H = \mathbf{I}_K$. The uplink pilot transmission power is set to $\tau\rho$. Therefore, the base station receives a $M \times \tau$ pilot matrix from M antennas

$$\mathbf{Y} = \sqrt{\tau\rho}\mathbf{G}\mathbf{\Psi} + \mathbf{N}, \tag{3.18}$$

where $\mathbf{N}$ represents the $M \times \tau$ noise matrix whose elements are i.i.d. $\mathcal{CN}(0,1)$. The MMSE estimate of $\mathbf{G}$ is

$$\hat{\mathbf{G}} = \frac{1}{\sqrt{\tau\rho}}\mathbf{Y}\mathbf{\Psi}^H\widetilde{\mathbf{D}} \tag{3.19}$$

where $\widetilde{\mathbf{D}} \triangleq (\frac{1}{\tau\rho}\mathbf{D}^{-1} + \mathbf{I_K})^{-1}$. The error matrix of estimation is defined as $\mathbf{\Delta} \triangleq \hat{\mathbf{G}} - \mathbf{G}$. Due to the property of MMSE estimator, $\hat{\mathbf{G}}$ and $\mathbf{\Delta}$ are independent and each element of the kth column of $\mathbf{\Delta}$ are random variables with zero mean and variance $\frac{\beta_k}{\tau\rho\beta_k+1}$. Therefore, by using the estimated channel $\hat{\mathbf{G}}^H$ for MRC detection, the received signal vector at the base station is:

$$\hat{\mathbf{r}} = \hat{\mathbf{G}}^H\left(\sqrt{\tau\rho}\hat{\mathbf{G}}\mathbf{x} - \sqrt{\tau\rho}\mathbf{\Delta}\mathbf{x} + \mathbf{w}\right), \tag{3.20}$$

Based on [6], the lower bound of achievable rate for the kth user using MRC can be expressed as:

$$R_k^{IP} = \log_2\left(1 + \frac{\tau\rho^2(M-1)\beta_k^2}{\rho(\tau\rho\beta_k+1)\sum_{i=1,i\neq k}^{K}\beta_i + (\tau+1)\rho\beta_k + 1}\right) \tag{3.21}$$

When $M \to \infty$, the asymptotic achievable rate of kth user is:

$$R_k^{IP} = \log_2(1 + \tau M \rho^2 {\beta_k}^2) \tag{3.22}$$

$$= \log_2(1 + \tau M \rho^2 \phi^2 r_k^{-2\alpha} \zeta_k^2) \tag{3.23}$$

Notice that the rate expression depends on squares of the large scale fading coefficient compared to the perfect CSI case. Since ζ_k is a lognormal random variable, we denote $\hat{\zeta}_k = \zeta_k^2$ that $\hat{\zeta}_k \sim 10\log_{10}\mathcal{N}(0, 4\sigma_k^2)$. Similar to (3.13), the maximum achievable rate $R_{k,\epsilon}^{IP}$ of the kth user under outage probability constraint ϵ is

$$R_{k,\epsilon}^{IP} = log_2(1 + \tau M \rho^2 \phi^2 r_k^{-2\alpha} 10^{0.2\sigma_k Q^{-1}(1-\epsilon)}). \tag{3.24}$$

Also the cell coverage area with imperfect CSI has the following expression

$$C^{IP} = Q(\hat{A}) + exp[2(\frac{1 - \hat{A}\hat{B}}{\hat{B}^2})]Q(\frac{2}{\hat{B}} - \hat{A}), \tag{3.25}$$

where

$$\hat{A} = \frac{5\log\frac{p_m c^{2\alpha}}{\tau M \rho^2 \phi^2}}{\sigma_k}, \hat{B} = \frac{10\alpha \log e}{\sigma_k}. \tag{3.26}$$

3.4 Multi-Cell Uplink Outage Analysis

In a multi-cell environment, consider a frequency reuse factor a, a set of L Cells share same frequency band also the same set of orthogonal pilots. During the uplink training phase, the base station in cell j receives pilot signals from both the intended user k and other cell users in the same frequency band. The other cell users reusing the same pilot sequence interfere with the transmission of kth user terminal to its own base station in cell j. This phenomenon is called pilot contamination[3]. Base station estimates the contaminated channel and treat it as the true channel, causing the subsequent detection compromised. It is show by[3], as the number of base station

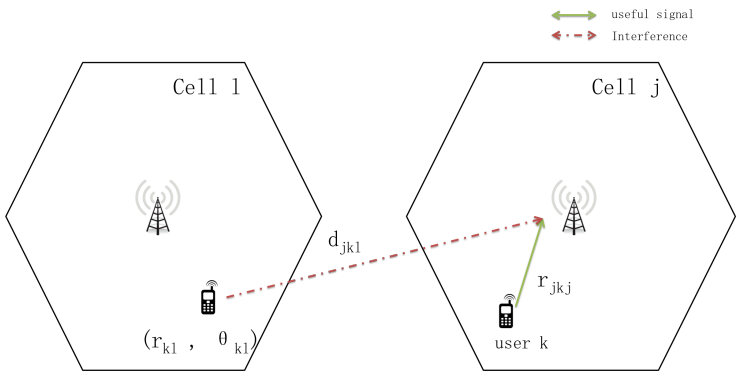

Figure 3.1. user k in cell j receives interference from another user in cell l reuse the same pilot signal.

antennas approaches to infinity, the small scale fading and uncorrelated noise vanished due to favorable propagation. The only interference caused by the pilot contamination limits the signal-to-interference ratio (SIR) for a multi-cell massive MIMO system. From the result obtained by [3], as $M \to \infty$ and using MRC detection, the effective SIR of kth user terminal in jth cell can be expressed as

$$SIR = \frac{\beta_{jkj}^2}{\sum_{l \neq j}^{N_I} \beta_{jkl}^2}. \tag{3.27}$$

Where β_{jkj} indicates the large scale fading coefficient from the kth user in jth cell to its own base station, β_{jkl} is the large scale fading coefficient from kth interfering user in lth cell to the base station in jth cell and N_I is the number of interference cells. Note that since the noise are average out, the multi-cell massive MIMO system is in the interference limited regime. Therefore SIR is abbreviated for SINR for clarity. The SIR equation shows that both the large scale fading coefficients of intended signal and interference signals are proportional to their squares caused by MRC processing.

Plug in (3.3) into the above equation, the SIR can be written as

$$SIR = \frac{r_{jkj}^{-2\alpha} \zeta_{jkj}^2}{\sum_{l \neq j}^{N_I} d_{jkl}^{-2\alpha} \zeta_{jkl}^2}. \tag{3.28}$$

Where r_{jkj} represents the distance of kth uplink user to its base station in cell j and d_{jkl} represents the distance of kth interference user from lth cell to the base station in cell j. Since we assume users are uniform distributed in each cell. Denote r_{kl} as the distance of kth interference user in cell l to its own base station, we use (r_{kl}, θ_{kl}) represents the interferer's polar coordinate. d_{jkl} in the denominator of SIR expression can be calculated as

$$d_{jkl} = \sqrt{r_{kl}^2 - 2sin\theta_{kl} r_{kl} D + D^2} \tag{3.29}$$

D represents the reuse distance from the base station in the cell of interest to the first tier interfering cell center that $D = \sqrt{3a}c$. In order to make outage analysis of the asymptotic rate of the kth user, we need to obtain the distribution of SIR. Conditioned on user location, we can observe that the denominator of SIR expression equals to a summation of independent lognormal random variables $\zeta_{jkl}^2 \sim 10\log_{10}\mathcal{N}(2\mu_{jkl}, 4\sigma_{jkl}^2)$. The interferers are assumed to be statistically identical[22] such that

$$\mu_{jkl} = \mu_I = 0, l = 1, 2, 3, ..., N_I \tag{3.30}$$

$$\sigma_{jkl} = \sigma_I, l = 1, 2, 3, ..., N_I \tag{3.31}$$

The above assumption holds when the interferers have the same distance $d_{jkl} = d_I$ to the base station in the jth cell of interest. Here we let $\widetilde{\zeta_{jkl}} = \zeta_{jkl}^2$ that $\widetilde{\zeta_{jkl}} \sim 10\log_{10}\mathcal{N}(2\mu_I, 4\sigma_I^2)$. Generally there's no closed form formula for the summation of log-normal random variables. However, it can be approximated by another log-normal random variable with chosen parameters which is known as the Fenton-Wilkinson Method[15]. Here we use Fenton's method for simplicity. We denote the approximation as

$$\Omega_I = \sum_{l=1}^{N_I} \widetilde{\zeta_{jkl}}. \tag{3.32}$$

Where $\Omega_I \sim 10\log_{10}\mathcal{N}(\mu_{\Omega_I}, \sigma^2_{\Omega_I})$. Applying Fenton's method, the mean μ_{Ω_I} and variance σ_{Ω_I} can be expressed as

$$\mu_{\Omega_I} = \frac{\kappa\left(4\sigma^2_{jkl} - \sigma^2_{\Omega_I}\right)}{2} + \frac{1}{\kappa}\ln\left(\sum_{l=1}^{N_I} e^{2\kappa\mu_{jkl}}\right), \tag{3.33}$$

$$\sigma^2_{\Omega_I} = \kappa^{-2}\ln\left(\left(e^{4\kappa^2\sigma^2_{jkl}} - 1\right)\frac{\sum_{l=1}^{N_I} e^{4\kappa\mu_{jkl}}}{\left(\sum_{l=1}^{N_I} e^{2\kappa\mu_{jkl}}\right)^2} + 1\right). \tag{3.34}$$

where $\kappa = (\ln 10)/10$. Plug in (3.30) (3.31) and $N_I = 6$ considering the first tier co-channel interferer, equation (3.33) (3.34) can be further simplified to

$$\mu_{\Omega_I} = \frac{1}{2\kappa}\ln\frac{6^3 e^{4k^2\sigma_I^2}}{e^{4k^2\sigma_I^2} + 5}, \tag{3.35}$$

$$\sigma^2_{\Omega_I} = \kappa^{-2}\ln\left(\frac{e^{4\kappa^2\sigma_I^2} + 5}{6}\right). \tag{3.36}$$

Since the numerator of SIR is also a lognormal random variable with $\widetilde{\zeta_{jkj}} = \zeta^2_{jkj}$, $\widetilde{\zeta_{jkj}} \sim \ln\mathcal{N}(2\mu_{jkj}, 4\sigma^2_{jkj})$. Therefore, the numerator divided by the denominator is also a lognormal random variable that $Z = \frac{\widetilde{\zeta_{jkj}}}{\Omega_I}$. We have

$$Z \sim 10\log_{10}\mathcal{N}(\mu_Z, \sigma^2_Z) \tag{3.37}$$

where $\mu_Z = -\mu_{\Omega_I}$ and $\sigma_Z^2 = 4\sigma_{jkj}^2 - \sigma_{\Omega_I}^2$.

Define ratio $\gamma = \frac{d_I}{r_{jkj}}$, the SIR in (3.28) can be rewritten as

$$SIR = \gamma^{2\alpha} Z \tag{3.38}$$

For a multi-cell uplink massive MIMO system, the maximum achievable rate $R_{k,j,\epsilon}^{Mul}$ of the kth user in jth cell under outage probability constraint ϵ is

$$R_{k,j,\epsilon}^{Mul} = log_2(1 + \gamma^{2\alpha} 10^{0.1\left(\sigma_Z Q^{-1}(1-\epsilon)+\mu_Z\right)}) \tag{3.39}$$

The cell coverage area of a multi-cell massive MIMO user is then

$$C^{Mul} = Q(\widetilde{A}) + exp[2(\frac{1-\widetilde{A}\widetilde{B}}{\widetilde{B}^2})]Q(\frac{2}{\widetilde{B}} - \widetilde{A}), \tag{3.40}$$

where

$$\widetilde{A} = \frac{10\log\left((\frac{c}{d_I})^{2\alpha} p_m\right) - \mu_Z}{\sigma_Z}, \widetilde{B} = \frac{20\alpha \log e}{\sigma_Z} \tag{3.41}$$

3.5 Numerical results

In this section, we use numerical results to evaluate the uplink massive MIMO system performance affected by shadow fading. We assume cell radius $c = 800$. The path loss exponent α is set to 3.71. Equal transmit power of each user are assumed and the received SNR at 600m away from the transmitter is set to be 10dB. We assume $K = 7$ uplink users and the pilot length τ is set equal to K. The number of antennas M is set to be 200. The antenna gain ϕ is normalized to 1.

Firstly we study the performance of the single-cell system. Fig.3.2 shows the achievable rate of a user located 600m away from base station under outage constraint $\epsilon = 0.01$. With perfect CSI and imperfect CSI, the achievable rate drops gradually as the parameter σ, known as the dB spread, of log-normal distributed shadow fading

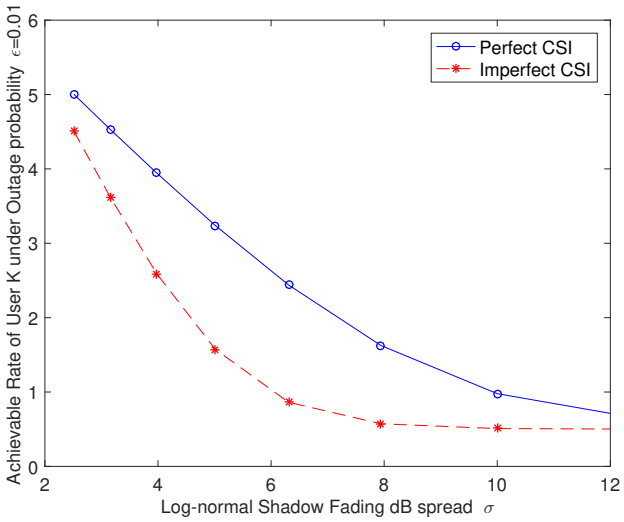

Figure 3.2. Single-cell achievable rate of user K under outage probability constraint $\epsilon = 0.01$ with perfect CSI and imperfect CSI..

increases. From the curve we can observe that the imperfect CSI case suffers more performance degradation than perfect CSI. For example, increasing σ from 4dB to 5dB brings a rate loss of 18% for perfect CSI and 30% for imperfect CSI. Fig.3.3 shows that, with a minimum SNR requirement $p_m = 6dB$, cell coverage ratio decreases for both perfect CSI and imperfect CSI cases but the one with imperfect CSI decreases slightly faster.

Fig.3.4 plots the cell coverage ratio for multi-cell uplink massive MIMO system with different frequency reuse factor $a = 1$ and $a = 3$. We can observe from the curve that with a larger frequency reuse factor, the coverage ratio significantly improved. This is due to the fact that interferers from other cells reusing the same pilot sequence are pushed further away from the target cell and the combining effect of path loss and shadow fading contributed to the interference is reduced. With a more aggressive frequency reuse, the coverage ratio has a prominent drop before σ reaches 7 and then decrease slowly when σ is large.

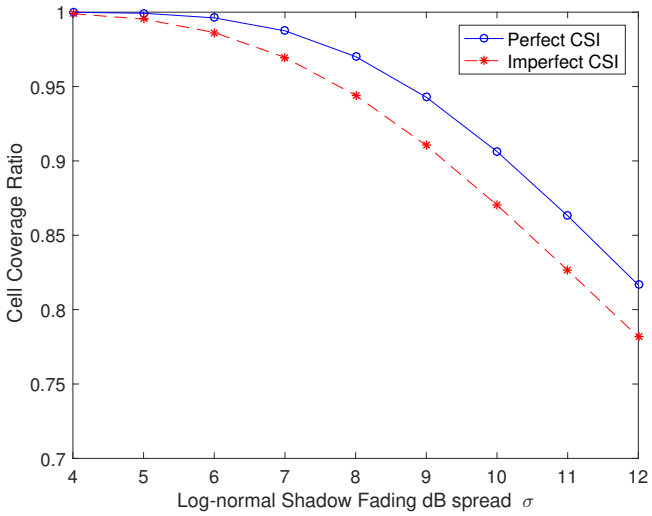

Figure 3.3. Single-cell coverage ratio with perfect CSI and imperfect CSI. Minimum received SNR requirement $p_m = 6dB$ and cell radius $c = 800$..

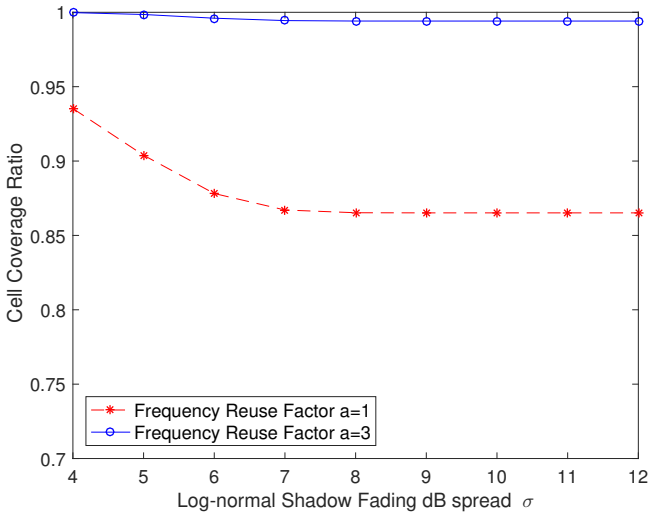

Figure 3.4. Multi-cell coverage ratio with frequency reuse factor $a = 1$ and $a = 3$. Minimum received SNR requirement $p_m = 6dB$ and cell radius $c = 800$..

3.6 Conclusions

In this paper, we make outage analysis of a multi-user uplink massive MIMO system. As the number of base station antennas goes large, small scale fading effect

vanishes and only large scale fading remains. Due to the randomness of log-normal distributed shadow fading, we derived the achievable rate and cell coverage area ratio under certain outage constraint for both single-cell and multi-cell scenarios. From the numerical result analysis, we conclude that shadow fading has significant impact on the performance in terms of the rate and coverage ratio metrics. For single-cell system, imperfect CSI caused by channel estimation error suffers more from shadow fading effect. Shadow fading also degrades the performance of multi-cell system with aggressive frequency reuse factor.

CHAPTER 4

An EMD based Sense-through-Foliage Target Detection Approach with UWB Radar Sensor Networks

4.1 Introduction

Target detection and identification in a strong background clutter is a significant topic of civilian and military research and applications. For example, in modern warfare, forest provides good cover of enemy military targets such as tanks, artillery and other weapon caches. Therefore, sense-through-foliage target detection is important for eliminating potential hostile enemy activities. However, the non-stationary nature of foliage environment, for example, doppler shift caused by tree leaves and branches blowing in the wind makes the target detection difficult. Despite of the dynamic and impulsive nature of background foliage clutter, it was also shown to be a rich scattering environment that multi-path propagation effects could dominate received echoes containing both target and clutter information[23].

In this paper, our goal is to make the target appear from the background foliage clutter based on our knowledge in signal processing and sensor networks using UWB radar. Compare to other types of signals used on foliage target detection study, such as waveforms used in UHF and VHF bands [24] to analyze attenuation and backscatter statistics of foliage and Millimeter-Wave radar [25] [26] used to detect target underneath foliage-cover, UWB radar operates at a relatively lower frequency band between 100MHz and 3GHz with a large fractional bandwidth greater than 20 percent. With such characteristics UWB radar is more suited for short distance

application. However, the good penetration ability also high range resolutions make UWB radar has more advantage than narrow band signals in terms of target detection.

Some previous works related to sense-through-foliage target detection using UWB radar have been conducted. In [27], DCT based approach is proposed to detect target through foliage. [28] proposed differential and STFT based sense-through-foliage approach. Meanwhile, some information theory based methods using mutual information [29] and relative entropy [30] [31] are applied in this topic. Also intensive studies can be found in literature[32][33][34][35][36][37][38]. Due to the characteristic of foliage which makes it difficult to use conventional time-frequency analysis to extract features of radar echoes, we are inspired by Empirical Mode Decomposition (EMD) for it has been widely used to analyze non-stationary and nonlinear signals. EMD decomposes multi-component signals into several frequency components know as intrinsic mode functions (IMFs) and a trend function (residue) through a sifting process [39]. Some research works have employed EMD method to analyze radar target signal corrupted by sea clutter[40]. In [41] and [42], EMD based method are also applied to sense through wall human target detection which could be treated as an opposite scenario of sense-through-foliage since the human target has micro doppler shift due to breadth and heart beat while the background clutter (wall) is stationary. Also in [43] EMD is shown to act as a dyadic filter bank in stochastic situations involving broadband noise.

The rest of this chapter is organized as follows: In Section II, we introduce the measurement and data collection used in the paper. In Section III, we propose the EMD based sense-through-foliage target detection approach with good signal quality. In Section IV, the combined RAKE structure and sense-through-foliage target detection is discussed when the signal has poor quality. In Section V, we draw the conclusion.

4.2 Data measurement and collection settings

In this work, the experimental sense-through foliage data is from Air Force Research Lab[44]. The foliage penetration measurement effort began in late summer and continued through early winter. Late summer foliage involved in the measurement has decreased water content due to the limited rainfall. Here we use the data measured in November which involved late fall and winter largely defoliated but dense foliage.

The experiment was constructed on a seven-ton man lift with a total lifting capacity of 450 kg. The principle pieces of equipment secured on the lift are: Barth pulser, Tektronix model 7740B oscilloscope, dual antenna mounting stand, two antennas, rack system, IBM laptop, HP signal generator, custom RF switch and power supply and Weather shield (small hut). Throughout this work, a Barth pulse source (Barth Electronics, Inc. model 732 GL) was used. The pulse generator uses a coaxial reed switch to discharge a charge line for a very fast rise time pulse outputs. The model 732 pulse generator provides pulses of less than 50 picoseconds rise time, with amplitude from 150 V to greater than 2 KV into any load impedance through a 50 ohm coaxial line. The generator is capable of producing pulses with a minimum width of 750 ps and a maximum of 1 microsecond. This output pulse width is determined by charge line length for rectangular pulses, or by capacitors for 1/e decay pulses. The target is a trihedral shape metal reflector placed at 600 ft round trip distance from UWB bistatic antennas as show in Fig.4.1.

For the data used in this paper, each data collection contains 16,000 samples with a 50 picosecond sample interval for a total time duration of 0.8 microseconds at a rate of approximately 20 Hz. We considered two sets of data from this experiment. Initially, the Barth pulse source was operated at low amplitude and 35 pulses reflected signal were averaged for each collection. Significant pulse-to-pulse variability was noted for these collections. This collection is referred as "poor" signal quality data.

Figure 4.1. A trihedral metal target placed at 300 feet from the lift.

Later, good signal quality data were collected using higher amplitude pulses and 100 pulses reflected signals were averaged for each collection. This collection is referred as "good" signal quality data.

4.3 Empirical Mode Decomposition and Hilbert Transform

Empirical Mode Decomposition was introduced as part of Hilbert-Huang Transform(HHT) for non-stationary and non-linear signal time-frequency analysis[9]. The main idea of EMD is to decompose the given multi-component signal into a series of finite intrinsic oscillatory basic functions and a residue through the sifting process. These mono-component basic functions are called intrinsic mode functions (IMF) which satisfy two conditions: (1) the number of extrema (local maximum or local minimum) and the number of zero crossings are either equal or differ at most by one; (2) the average of the envelope defined by the local maxima and the envelope defined by the local minima is zero at all points [9].

Compared to other other time-frequency analysis techniques like Short-Time Fourier Transform (STFT) and wavelet transform, The EMD algorithm is not only a fully data-driven but also adaptive method. The STFT usually requires a suitable window size selection to match with the special frequency content of the signal which is not known a priori. The wavelet transform performance is greatly affected by the types of basic wavelet function employed [45]. Unlike these methods, the EMD does not require a priori basis functions and decompose the signal based on its intrinsic properties. The sifting process used in EMD of a given signal $x(t)$ is described as follows:

1. Identify all the extrema (local maxima and minima) of $x(t)$.
2. Interpolate the local maxima using cubic spline line to obtain the upper envelope denote as $e_{upper}(t)$. Repeat the same procedure for local minima to obtain the lower envelope $e_{lower}(t)$.
3. Calculate the mean of upper and lower envelope $m_1(t) = (e_{upper}(t) - e_{lower}(t))/2$.
4. Calculate the difference between $x(t)$ and $m_1(t)$ as $h_1(t) = x(t) - m_1(t)$.
5. Examine if $h_1(t)$ satisfy the two criteria of IMF. If it does not treat $h_1(t)$ as the original signal $x(t)$ and repeat step1 - step4. Denote the the mean of upper and lower envelopes constructed from the extrema from $h_1(t)$ as $m_{11}(t)$. Then the difference between $h_1(t)$ and $m_{11}(t)$ is given as $h_{11}(t) = h_1(t) - m_{11}(t)$. Repeat this process k times until $h_{1k}(t) = h_{1(k-1)} - m_{1k}(t)$ meets the IMF criteria. Then the first IMF is extracted from the signal and designated as $c_1(t) = h_{1k}(t)$. However, to guarantee the extracted IMFs has enough physical meaning, a Cauchy type stop criterion is introduced to stop the sifting process by limiting the standard deviation computed from two consecutive sifting results as the following[46]:

$$SD = \sum_{t=0}^{T} \left[\frac{\left| h_{1(k-1)}(t) - h_{1k}(t) \right|^2}{h_{1(k-1)}^2}(t) \right] \tag{4.1}$$

Typical value for SD can be set between 0.2 and 0.3 [46].

6. Subtract $c_1(t)$ from the the rest of signal $x(t)$, the residue $r_1(t) = x(t) - c_1(t)$ is treated as signal $x(t)$ and repeat step1 - step5 n times to extract the rest IMFs from $c_2(t)$ to $c_n(t)$.

$$r_2(t) = r_1(t) - c_2(t)$$

...

...

$$r_n(t) = r_{n-1}(t) - c_n(t)$$

The sifting process ends until no IMF can be obtained from the residue $r_n(t)$ which means that $r_n(t)$ becomes a monotonic function. Therefore the original signal can be represented by all the extracted IMFs and the residue as:

$$x(t) = \sum_{i=1}^{n} c_j(t) + r_n(t) \tag{4.2}$$

Since the extracted intrinsic mode functions can be seen as monocomponent signals, it is straightforward to compute the Hilbert transform for each IMF to construct analytical signal which has meaningful instantaneous frequency. The $\hat{c_j}(t)$ denotes the complex conjugate of the real valued signal $c_j(t)$ can be determined as:

$$\hat{c_j}(t) = \mathcal{H}[x(t)] = \frac{1}{\pi} p.v. \int_{\infty}^{-\infty} \frac{x(\tau)}{t - \tau} d\tau, \tag{4.3}$$

Where $p.v.$ indicates the Cauchy principal value. The analytical signal obtained from each IMF is then defined as:

$$s_j(t) = c_j(t) + i\hat{c_j}(t) = a_j(t) e^{i\theta_j(t)}, \tag{4.4}$$

where

$$a_j(t) = \sqrt{c_j^2 + \hat{c_j}^2}, \tag{4.5}$$

$$\theta_j(t) = arctan(\frac{\hat{c_j}}{c_j}). \tag{4.6}$$

$a_j(t)$ denotes the instantaneous amplitude and $\theta_j(t)$ is denotes the phase function. The instantaneous frequency is:

$$\omega_j = \frac{d\theta}{dt} \tag{4.7}$$

After performing the Hilbert transform for each IMF component, the original signal can be expressed as the real part of the following:

$$x(t) = \Re \left\{ \sum_{j=1}^{n} a_j(t) e^{\left[i \int \omega_j(t) dt \right]} \right\} \tag{4.8}$$

Then we are able to calculate the Hilbert spectrum $\mathcal{H}(\omega, t)$ as the frequency-time distribution of the amplitude.

4.4 Sense-through-foliage target detection with good signal quality using EMD approach

In Fig.4.2, we plot the two collections of data with good signal quality. Fig.4.2(a) shows the ones without target on range and Fig.4.2(b) shows the received echoes with target appears around sample 13,900. To gain a more clear view, we provide the expanded views of Fig.4.2 from sample 13,001 to 15,000 as plotted in Fig.4.3(a) without target and Fig.4.3(b) with target respectively. Since the Fig.4.3(a) has no target on range, it can be treated as the pure background clutter response. Therefore, It is intuitively to calculate the echo difference between Fig.4.3(a) and Fig.4.3(b) which is the result shown in Fig.4.3(c). From Fig.4.3(c) we can observe that target appears at around sample 14,000. However, practically it is impossible for us to obtain both col-

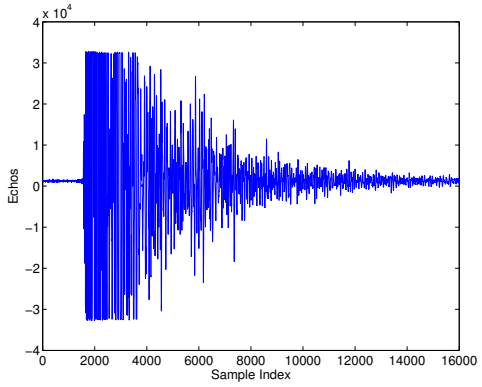

(a)

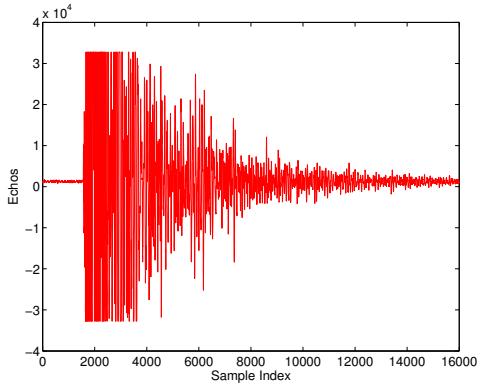

(b)

Figure 4.2. Measurement with very good signal quality and 100 pulses average. (a) No target on range, (b) with target on range (target appears at around sample 13,900) .

lection of data(Fig.4.3(a) and Fig.4.3(b)) simultaneously. We can only detect target based on only one of them(Fig.4.3(a) or Fig.4.3(b)).

The real world data usually tends to be non-stationary in nature. Motivated by this, we apply the EMD algorithm to our two collections of data to see if any useful information about the target can be extracted. Since the EMD is an iterative algorithm which is time consuming, in this paper, by comparing the results using different stopping criteria, we confine the each sifting process to 10 iterations and the obtained result is good enough to conduct target detection task. After applying

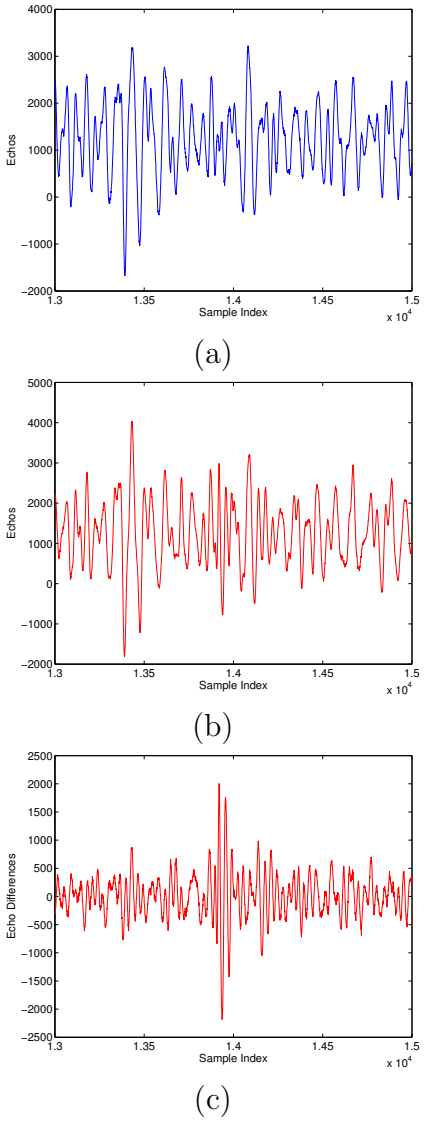

Figure 4.3. Measurement with very good signal quality and 100 pulses average. (a) Expanded view of traces (with target) from samples 13,001 to 15,000. (b) Expanded view of traces (without target) from samples 13,001 to 15,000. (c) Echo differences between (a) and (b).

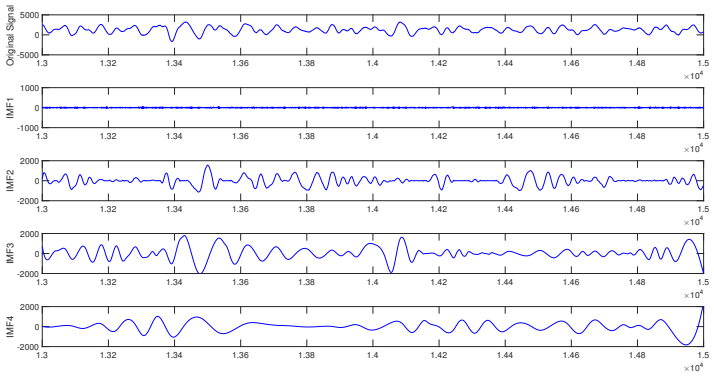

(a)

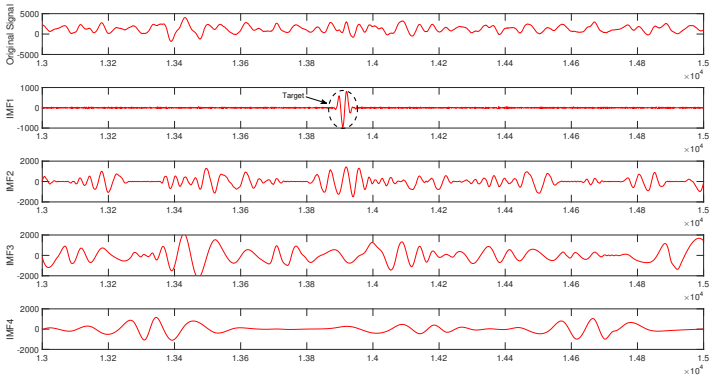

(b)

Figure 4.4. EMD results with good signal quality. (a) Original signal and IMF1-4 with no target on range, (b) Original signal and IMF1-4 with target on range (Observed target signature in IMF1 at around sample 13,900).

EMD for samples provided in Fig.4.3(a) and Fig.4.3(b), we plot the first three order IMFs extracted from the sifting process in Fig.4.4.

Observe in Fig.4.4(b) which is the EMD result of echoes with target, the first IMF which contains the highest frequency component of original signal has a higher amplitude oscillation at around sample 14,000 compared to other sample locations. Due to the fact that the foliage clutter is very impulsive and behaves like Gaussian distributed noise [27] in the frequency domain, it is impossible to separate target and

noise in each IMF which means each IMF contains both information about target and foliage clutter. However, in the first IMF sample locations other than sample around 13,900 have low amplitude fluctuation and behaves like Gaussian noise. We can conclude that the high energy oscillation around sample 13,900 in IMF1 is the signature of the target and this also imply higher signal to clutter ratio (SCR) in high frequency. We also plot the IMFs extracted from the signal without target as shown in Fig.4.4(a) that in the first IMF we didn't notice any obvious change in all samples and this can represent the foliage clutter feature. This also proved our conclusion by comparing the two figures. Fig.4.5 is the Hilbert Spectrum of the original signal.

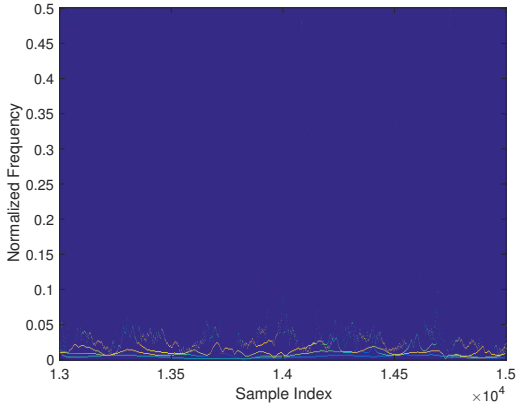

Figure 4.5. Hilbert spectrum of original signal.

4.5 Sense-through-foliage target detection with poor signal quality using RSN and EMD approach

As mentioned in Section II, when the Barth pulse source was operated at low amplitude, the sample values are not obtained based on sufficient pulse response averaging (averaged over 35 pulses for each collection) and this results in poor return signal quality. We plot the two collections of data with poor signal quality in

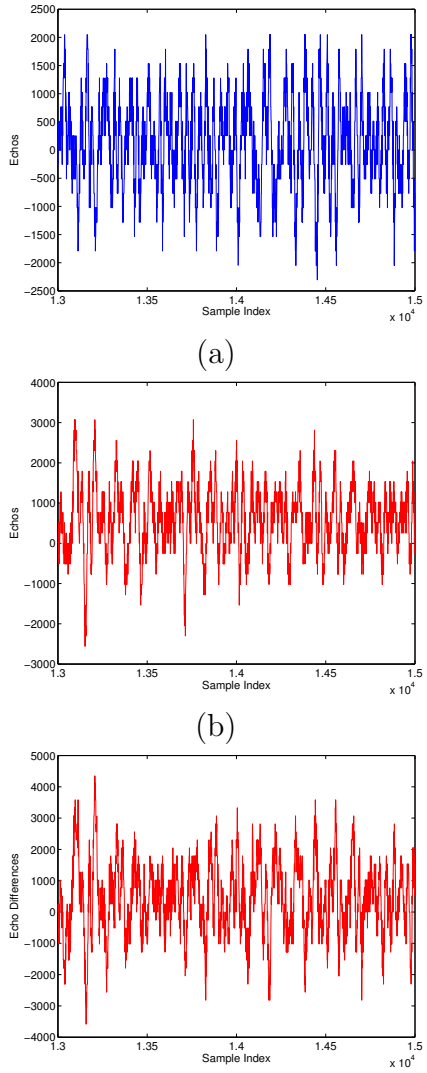

Figure 4.6. Measurement with poor signal quality and 35 pulses average. (a) Expanded view of traces (no target) from sample 13,001 to 15,000. (b) Expanded view of traces (with target) from sample 13,001 to 15,000. (c) The differences between (a) and (b). .

Fig.4.6(a) without target, Fig.4.6(b) with target on range and Fig.4.6(c) the difference between two data collections. From Fig.4.6(c) we are not able to tell whether there's the target. Also, in Fig.4.7(a) and Fig.4.7(b) we draw the extracted IMFs results using EMD approach from these two data collections. From the high frequency

IMFs we are not able to observe any noticeable target signature. However, significant pulse-to-pulse variability is observed in the UWB radar receive echoes. This motivate us to explore the spatial and time diversity using Radar Sensor Networks (RSN).

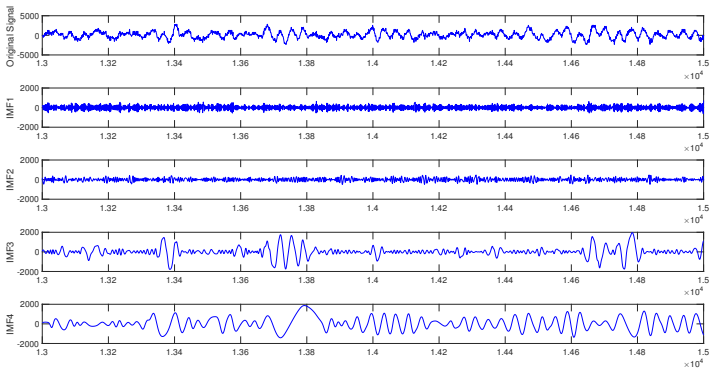

(a)

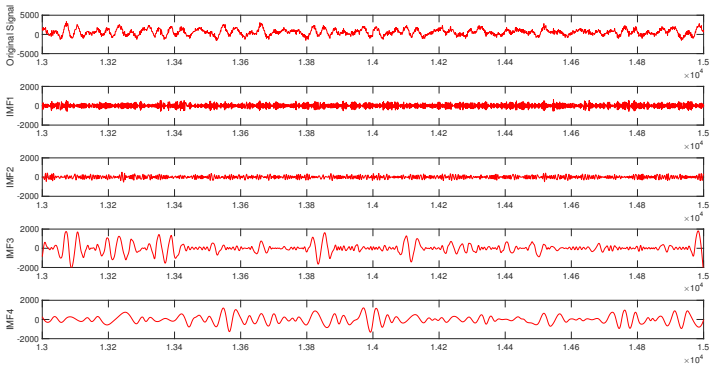

(b)

Figure 4.7. EMD results with poor signal quality. (a) Original signal and IMF1-4 with no target on range, (b) Original signal and IMF1-4 with target on range. .

In this case, we propose to use a RAKE structure to handle poor signal quality target detection problem. RAKE structure is an effective diversity combining method due to the fact that uncorrelated radar measurements could experience different fading levels. Echoes from different cluster-member radars are combined by the cluster head.

We consider two different diversity combing schemes to implement Rake structures: equal gain combing and maximum ratio combining. The equal gain combined signal can be formulated as the following:

$$x_{eq}(n) = \frac{1}{M} \sum_{i=1}^{M} x_i(n). \tag{4.9}$$

Here M is the number of radar echoes used in the combining.

The maximum ratio combing scheme uses a weighted average w_i determined by the power of each echo $x_i(n)$ (n is the sample index),

$$E_i = \text{var}(x_i(n)) + [\text{mean}(x_i(n))]^2, \tag{4.10}$$

where

$$w_i = \frac{E_i}{\sum_{i=1}^{M} E_i}. \tag{4.11}$$

The maximum ratio combined signal has following form:

$$x_{mrc}(n) = \sum_{i=1}^{M} w_i x_i(n) \tag{4.12}$$

After the diversity combing EMD is applied to the combined signal. We plot the IMFs extracted from two cases in Fig.4.9(a) (without target) and Fig.4.9(b) (with target). In Fig.4.9(b), from first IMF with highest frequency component, we cannot tell if there's a target. However, in the second IMF with second highest frequency, we observed a high amplitude oscillation around sample 14,000. Also in Fig.4.9(a) which represents the IMFs of foliage clutter we do not observe anything in the first two IMFs. Therefore, we conclude this high amplitude oscillation in IMF2 is the target signature. This observation also in accordance with the result of target detection of good quality signal.

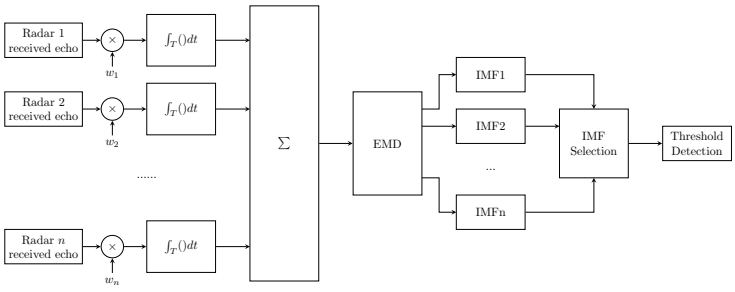

Figure 4.8. Block diagram of RAKE struture.

In our database, totally 70 radar echoes can be used to construct the Rake structure receiver. We further investigates the RAKE structure performance at different combing levels. For example, we randomly choose $M = 10$, $M = 20$ and $M = 30$ radar echoes in the database and 10,000 Monte Carlo simulations are performed at each combing level. Fig.4.10 shows the probability of detection with different thresholds for equal gain combing and maximum ration combing scheme. From the figure we can see that the maximum ratio combing method outperforms equal gain combing method at each combing level. Using more radars also improves the detection accuracy.

4.6 Conclusions

In this paper, we proposed an EMD based approach for sense-through-foliage target detection. After extracted IMFs from the original signal through sifting process, we are able to observe target signature in the first IMF which represents the highest frequency component when the signal quality is good. When the signal quality is poor and a single collection of radar echo cannot carryout target detection, a

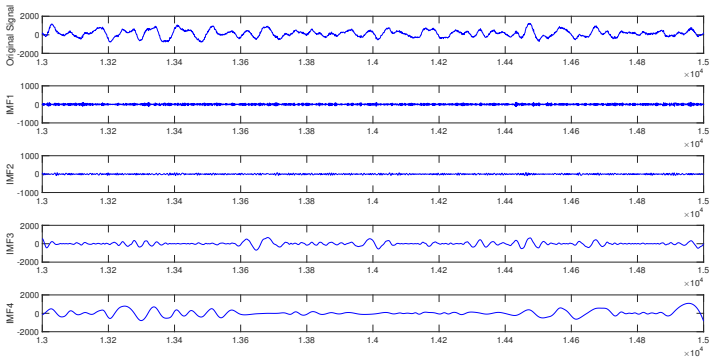

(a)

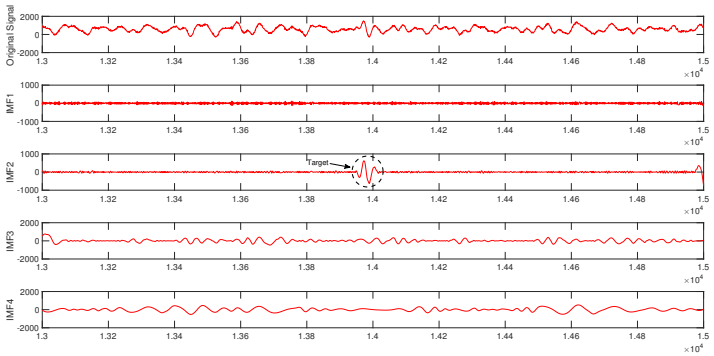

(b)

Figure 4.9. EMD results with poor signal quality after RAKE structure combing. (a) Original signal and IMF1-4 with no target on range, (b) Original signal and IMF1-4 with target on range. (Observed target signature in IMF2 at around sample 14,000).
.

RAKE structure in RSN using cluster-head radar by combining echoes from different cluster-member radars is used for preprocessing before applying EMD algorithm. From the second extracted IMF we are able to find similar target signature as the one appears in good quality signal. From the observation we also conclude that the signal-to-clutter ratio (SCR) in this sense-through-foliage scheme is significant in high frequency components of the original signal.

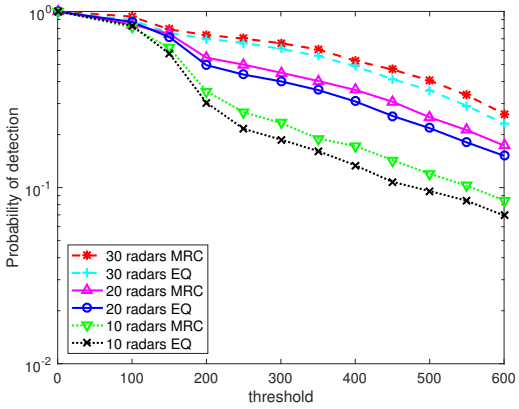

Figure 4.10. Probability of detection using maximum ratio combing and equal gain combing at radar combing level $M = 10$,$M = 20$ and $M = 30$.

CHAPTER 5

UWB Radar Target Detection using Hidden Markov Models

5.1 Introduction

In this chapter we propose a target detection and classification approach using Hidden Markov Models (HMMs). Hidden Markov Model is used as an classifier to distinguish between the presence of target in a background clutter and the pure clutter response. Two sets of features including common descriptive statistic features and radar signal features are extracted. Features have less correlation to each other are selected based on the feature covariance matrix and feed them into Hidden Markov Model for training. Sense-through-foliage target detection and Sense-through-Wall human detection are conducted using real world Ultra Wide Band (UWB) data. Experiment results show HMM based method provides good detection and false alarm rate for poor quality radar echoes in position 1 in the sense-through-foliage target detection scenario. Sense-through-wall human experiment results shows Hidden Markov Model based method could successfully detect stationary human targets using 2 states HMMs, but with a lower detection accuracy distinguish between stationary human and human with hand motion. Parameters are also investigated for HMMs to optimally model UWB radar signals.

Radar target detection is an important technique in remote sensing research and homeland security applications. The returned echoes from unwanted objects (known as clutter) such as ground, sea, trees, buildings and atmospheric turbulences and can often made the real target fade into the environment and complicates the detection task. For example, clutter echoes can contain much more power than target

echoes and threshold based detection method may result in high false alarms rate. In practical situations, warfighters on the battleground are always facing unknown non-line-of-sight enemy threats from covers. Law enforcement and rescue missions are confronted with situation to identify life signals behind walls and ruins. Therefore, increasing target detection accuracy is of great importance for these applications.

In this work, we deal with both sense-through-foliage and sense-through-wall target detection problems. Considering the non-stationary nature of foliage environment, doppler spread induced by clutter motion and multi-path clutter backscattering can degrade detection performance. We further consider a more challenging situation that data collected from radar sensors is not perfect, for example, poor quality echo signal. Sense-through-wall human detection relies on capturing doppler shift caused by micro motion (e.g. human breath and chest movement) and movement[51]. However, irregular contour of human bodies made themselves not perfect radar signal reflectors. Good signal reflectors like metallic objects return signals usually have dominant path.

UWB radar is characterized by a large instantaneous fractional energy bandwidth and waveforms formed by pulses with very short duration[52]. Good penetration ability and high range resolutions make UWB radar a good candidate for target detection behind clutter.

Hidden Markov model as a dynamic bayesian network (DBN) is a statistical model used to model temporal data and especially have great success on like speech recognition[53] [54], text classification [55] [56], machine translation[57] and other pattern recognition applications[58] [59] [60]. Recently, Hidden Markov Model based method have been applied to variant pattern recognition problems including radar target detection, classification and tracking problems since radar signal is essentially temporal. Hidden Markov Model models a stochastic process with a sequence of

observations produced by a underlying unobserved states transitions. The states are "Hidden" and follows a Markov process. Compared to deterministic model, Hidden Markov Model has rich mathematical foundation and model the signal as a parametric random process. The parameters of such random process can be precisely estimated using well-defined algorithms. In this paper, we propose to use Hidden Markov Model based method for UWB radar target detection by constructing HMMs for target and non-target case. The results presented by this paper provides validation and performance evaluation of using such method for radar target detection. The testing data are real world collected UWB radar data and experiment result shows that Hidden Markov Model is a good candidate for UWB radar target detection task. Furthermore, HMM parameters are studied for optimally model UWB radar signals.

The rest of this chapter is organized as follows: In Section II, we introduce the background knowledge of Hidden Markov Models. In Section III, we propose the HMM based target detection approach. In Section IV, we provide experiment results obtained by two sets of UWB testing data. In Section V, we draw the conclusion.

5.2 Introduction to Hidden Markov Model

Hidden Markov Model(HMM) was firstly introduced in the late 1960s and have gained increasing popularity for a wide rage of applications. By characterizing the statistical properties of the signal model, HMMs can be used to model both stationary or non-stationary random process. Generally, an HMM consists of two random processes. The first process has dimension of time which is essentially a first order Markov chain with N finite states defined by

$$S = \{S_1, S_2, ..., S_N\} \tag{5.1}$$

In the second random process, each state produces an observation result which is directly visible. However, the states are "Hidden" and not observable. In other words, we cannot directly tell the exact state where the observation occurs. The T observation symbols per state is

$$O = \{O_1, O_2, ..., O_T\} \tag{5.2}$$

A basic HMM is characterized by three sets of parameters, we use q_t represents the state of system and v_t represents the observation symbols at time t:

1. Initial state probability distribution matrix $\pi = \{\pi_i\}$, where each element $\pi_i = P(q_1 = S_i), 1 \leq i \leq N$ is the probability that the system is in state i at initial time $t = 1$.
2. State transition probability distribution matrix $A = \{a_{ij}\}$, where $a_{ij} = P(q_t = S_j \mid q_{t-1} = S_i), 1 \leq i, j \leq N$ is the probability that the system is in state j at time t given that the system is in state i at time $t - 1$.
3. Observation symbol probability distribution matrix $B = \{b_j(t)\}$, where $b_j(t) = P(v_t = O_t \mid q_t = S_j), 1 \leq j \leq N, 1 \leq t \leq T$ is the probability that the output observation symbol is O_t given the system is in state j at time t.

The notation $\lambda = \{A, B, \pi\}$ denotes a complete parameter set of HMM. In addition, if the observation symbol probability density function is discrete, a HMM is called Discrete Hidden Markov Model. Otherwise, it is called Continuous Hidden Markov Model. For continuous case, the states transition probability density functions are typically represented as a form of Gaussian mixtures[61][62][63][64].

HMM has been proven useful to solve real world problems, which can be categorized into three basic categories[53]:

1. Evaluation. Compute the probability of an observation sequence $P(O \mid \lambda)$ given a model $\lambda = (A, B, \pi)$. One possible solution for calculating $P(O \mid \lambda)$ is by

summing the joint distribution $P(O, Q \mid \lambda)$ over every possible state sequences based on Bayesian method,

$$\begin{aligned} P(O \mid \lambda) &= \sum_{Q} P(O, Q \mid \lambda) P(Q \mid \lambda) && (5.3) \\ &= \prod_{t=1}^{T} P(O_t \mid q_t, \lambda) \prod_{t=1}^{T} P(q_t \mid q_{t-1}, \lambda) && (5.4) \\ &= \sum_{q_1, q_2, \ldots q_T} \pi_{q_1} b_{q_1}(O_1) a_{q_1 q_2} b_{q_2}(O_2) \ldots a_{q_{T-1} q_T} b_{q_T}(O_T) && (5.5) \end{aligned}$$

This brute force computing method involves the order of $2TN^T$ calculations which is not practical to satisfy real application demand[65]. Fortunately, an alternative approach called forward algorithm can efficiently compute $P(O \mid \lambda)$ with much lower complexity of $O(N^2T)$. Defining forward probability $\alpha_t(j)$ as the probability of being in state j after observing first t partial observation symbols $O_1, O_2, \ldots O_t$:

$$\alpha_t(j) = P(O_1, O_2, \ldots O_t, q_t = S_j \mid \lambda) \tag{5.6}$$

$\alpha_t(j)$ can be solved using an inductive fashion in three steps:

(a) Initialization:

$$\alpha_1(j) = \pi_j b_j(O_1) \quad 1 \leq j \leq N \tag{5.7}$$

(b) Recursion:

$$\alpha_t(j) = \sum_{i=1}^{N} \alpha_{t-1}(i) a_{ij} b_j(O_t) \quad 1 \leq j \leq N, 1 \leq t \leq T \tag{5.8}$$

(c) Termination:

$$P(O \mid \lambda) = \sum_{i=1}^{N} \alpha_T(i) \tag{5.9}$$

2. Decoding. Find an optimal hidden state sequence S associate with an observation sequence O given a model $\lambda = (A, B, \pi)$. There are several criteria to define the "optimal" sequence. The most widely used criteria is find the state sequence that maximize the $P(Q, O \mid \lambda)$ by employing the Viterbi Algorithm[66].
3. Learning. Estimate model parameters $\lambda = (A, B, \pi)$ to maximize the probability of given observation sequence $P(O \mid \lambda)$. To find the optimal parameters of the HMM associate with the observation sequence is difficult and there"s no way to analytically find the optimal estimation. However, $P(O \mid \lambda)$ can be locally maximized using the Baum-Welch algorithm[67] [68]to efficiently find the maximum likelihood estimation of model parameters. Baum-Welch algorithm is essentially a special case of the Expectation-Maximization algorithm using iterative estimation approach given a initial guess of the probabilities. In each iteration a better estimation are computed to guarantee that $P(O \mid \hat{\lambda}) > P(O \mid \lambda)$ until the algorithm converges. To describe the Baum-Welch algorithm, we firstly needs to define a backward probability $\beta_t(i)$ as the probability of given the system being in state j at time t after observing partial observation symbols $O_{t+1}, O_{t+2}, ...O_T$ from $t+1$ to the end:

$$\beta_t(i) = P(O_{t+1}, O_{t+2}, ...O_T \mid q_t = S_i, \lambda) \tag{5.10}$$

Similar to the forward probability, $\beta_t(i)$ can also be computed inductively:

(a) Initialization:

$$\beta_T(i) = 1 \quad 1 \leq i \leq N \tag{5.11}$$

(b) Recursion:

$$\beta_t(i) = \sum_{j=1}^{N} a_{ij} b_j(O_{t+1}) \beta_{t+1}(j) \quad 1 \leq j \leq N, 1 \leq t \leq T \tag{5.12}$$

Before estimation of parameter A and B, a probability $\xi_t(i,j)$ is defined as the probability of being in state i at time t and state j at time $t+1$, given the observation and the model:

$$\xi_t(i,j) = P(q_t = S_i, q_{t+1} = S_j \mid O, \lambda) \tag{5.13}$$

and can be computed using forward and backward probabilities as:

$$\xi_t(i,j) = \frac{P(q_t = S_i, q_{t+1} = S_j, O \mid \lambda)}{P(O \mid \lambda)} \tag{5.14}$$

$$= \frac{\alpha_t(i) a_{ij} b_j(O_{t+1}) \beta_{t+1}(j)}{\sum_{i=1}^{N} \sum_{j=1}^{N} \alpha_t(i) a_{ij} b_j(O_{t+1}) \beta_{t+1}(j)} \tag{5.15}$$

Another probability $\gamma_t(j)$ is also defined as the probability being in state S_j at time t given the observation and model:

$$\gamma_t(j) = P(q_t = S_j \mid O, \lambda) \tag{5.16}$$

which can be computed as

$$\gamma_t(j) = \frac{P(q_t = S_j, O \mid \lambda)}{P(O \mid \lambda)} \tag{5.17}$$

$$= \frac{\alpha_t(j) \beta_t(j)}{\sum_{j=1}^{N} \alpha_t(j) \beta_t(j)} \tag{5.18}$$

The EM algorithm can be used to reestimate the model parameter A and B after initialization. Each iteration can be divided in to E-step(Expectation) and M-step(Maximization):

E-step:

1. Recursively compute $\alpha_t(j)$ and $\beta_t(j)$
2. Compute $\xi_t(i,j)$ and $\gamma_t(j)$

M-step:

Reestimate a_{ij} and b_{ij}

1.

$$\hat{a}_{ij} = \frac{\sum_{t=1}^{T-1} \xi_t(i,j)}{\sum_{t=1}^{T-1} \sum_{k=1}^{N} \xi_t(i,k)} \tag{5.19}$$

2.

$$\hat{b}_j(v_k) = \frac{\sum_{t=1,s.t.O_t=v_k}^{T} \gamma_t(j)}{\sum_{t=1}^{T} \gamma_t(j)} \tag{5.20}$$

5.3 Hidden Markov Model Based UWB Radar Target Detection

In our work, our task is to detect target in background clutter using UWB radar echoes. To tackle with this problem using Hidden Markov Model based method, Baum-Welch algorithm is firstly used to train different HMMs for both target and no target respectively. Then the testing sequences can be feed into each HMM to obtain a likelihood for each model. The decision of whether target is present or not is based on which model the testing sequence scores a higher likelihood. The detection method is shown in Fig.5.1.

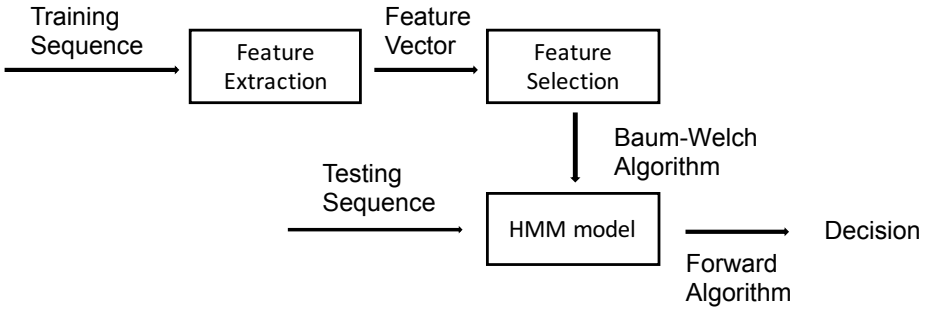

Figure 5.1. block diagram of HMM based target detection.

5.3.1 Feature Extraction and Selection

To provide effective input sequences for HMM training, we need to extract features that can well represent the target signature. Firstly, based on prior knowledge, a small range of signal around target on-site location should be carefully chosen. The selected signal is evenly divided into K windows. The number of windows K cor-

responds to the number of observations described in the last section. The temporal progression of these individual windowed signal can be seen as the result of hidden states transitions. Furthermore, in each window, two sets of features using time-frequency analysis are extracted to form a feature vector. The first set of features are some common statistics, for example, mean, variance, skewness, kurtosis, entropy, Dickey-Fuller test etc. Another feature set represents signal characteristics such as peak to peak ratio, crest factor, energy, RMS, number of abrupt changes, number of small changes, mean frequency etc. We denote the feature vector of the ith window as $\boldsymbol{X^i} = (X_1^i, X_2^i, ..., X_L^i)^T$ where L is the number of extracted features. We normalize the elements of feature vectors $\boldsymbol{X}$ between $[-1, 1]$ to ensure they have comparable magnitude in order to guarantee good estimation result. Fig.5.2 shows signals are divided into windows.

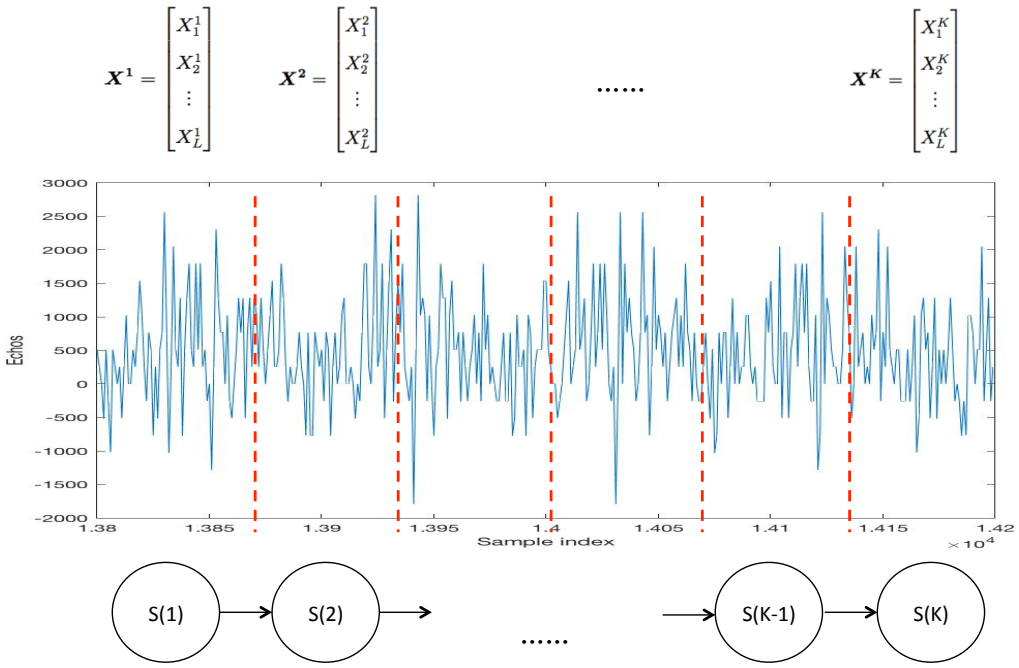

Figure 5.2. signal are evenly divided into K windows and L features are extracted with respect in each window.

Usually, the manually picked feature set may not be an efficient presentation of the radar signals, for example, two or more features could be mutually correlated resulting possible redundancy in the feature set. The elimination of features redundancy can be done by many different criteria. In this paper, we choose to eliminate features based on their covariance matrix

$$\Sigma_{ij} = cov(X_i, X_j) = \frac{E[(X_i - \mu_{X_i})(X_j - \mu_{X_j})]}{\sigma_{X_i}\sigma_{X_j}} > \delta \tag{5.21}$$

where δ is the threshold. We select l features with less cross correlation to others. The feature relevance can also be evaluated using mutual information [69].

5.3.2 Model Selection

Hidden Markov Models provide versatile modeling structures. For applications associate with different physical processs, designing proper HMM topology is crucial for successful presentation of modeled signal. Most commonly used HMMs are ergodic and left-right (Bakis) models [70] shown in figure X. The ergodic model has the property that every state can be reached from other states which means the state transition matrix $\boldsymbol{A}$ has no zero elements. The left-right model is particularly used to model signal properties change over time, for example, speech signals. The left-right model has the assumption that the states transition only occurs from lower order states to higher order states but not vice versa. To model radar target signals using HMM, the states transitions reflect radar range profiles of reflected energy and the progression of the radar echoes may contain information transferred between clutter and target. Therefore, an ergodic states transition model is more suitable to model radar signals.

5.3.3 HMM training and target detection

After selected l features used to represent signal profile in each window, these feature vectors of different windowed signals $\boldsymbol{X} = \{\boldsymbol{X}^1, \boldsymbol{X}^2, ..., \boldsymbol{X}^T\}$ can be treated as distinctive observation sequences for the input of Hidden Markov model training. To use discrete HMM, the feature vectors need to be quantized as discrete symbols using certain codebook . However, quantization may cause performance degradation due to the lost of precision. We implement continuous HMM assuming that the observation sequences are drawn from a mixture of M l-dimensional multivariate Gaussian densities. An M-component Gaussian mixture model has the form:

$$
\begin{aligned}
b_j(\boldsymbol{X}^t) &= P(\boldsymbol{X}^t \mid S_j) && (5.22)\\
&= \sum_{m=1}^{M} w_{jm} \mathcal{N}(\boldsymbol{\mu}_{jm}, \boldsymbol{U}_{jm}), && (5.23)\\
1 &\leq j \leq N, 1 \leq m \leq M, 1 \leq t \leq T && (5.24)
\end{aligned}
$$

where w_{jm} is the weight parameter of the mth mixture. $\mathcal{N}$ indicates a multivariable Gaussian density function:

$$
\mathcal{N}(\boldsymbol{\mu}, \boldsymbol{U}) = \frac{1}{(2\pi)^{l/2} |\boldsymbol{U}|^{1/2}} \exp\left(-\frac{1}{2}(\boldsymbol{X}^t - \boldsymbol{\mu})^T \boldsymbol{U}^{-1} (\boldsymbol{X}^t - \boldsymbol{\mu})\right) \tag{5.25}
$$

with l mean vector $\boldsymbol{\mu}_{jm}$ and $l \times l$ covariance matrix $\boldsymbol{U}_{jm}$ for the mth mixture in state j. T denotes transpose. The weight parameters c_{jm} has the constraint:

$$
\sum_{m=1}^{M} w_{jm} = 1, 1 \leq j \leq N, 1 \leq m \leq M \tag{5.26}
$$

Therefore, the a set of parameters $\lambda = \{A, w_{jm}, \mathcal{N}(\boldsymbol{\mu}_{jm}, \boldsymbol{U}_{jm}), \pi\}$ can be used to denote a continuous HMM with Gaussian mixture observation matrix. For continuous HMM, the parameter reestimation formula is given by[53]:

$$\hat{w_{jm}} = \frac{\sum_{t=1}^{T} \gamma_t(j,m)}{\sum_{t=1}^{T}\sum_{m=1}^{M} \gamma_t(j,m)} \tag{5.27}$$

$$\hat{\boldsymbol{\mu}}_{jm} = \frac{\sum_{t=1}^{T} \gamma_t(j,m)\boldsymbol{X^t}}{\sum_{t=1}^{T} \gamma_t(j,m)} \tag{5.28}$$

$$\hat{\boldsymbol{U}}_{jm} = \frac{\sum_{t=1}^{T} \gamma_t(j,m)(\boldsymbol{X^t} - \boldsymbol{\mu_{jm}})(\boldsymbol{X^t} - \boldsymbol{\mu_{jm}})^T}{\sum_{t=1}^{T} \gamma_t(j,m)} \tag{5.29}$$

where $\gamma_t(j,m)$ is the probability of being in state j at time t with the mth mixture component for $\boldsymbol{X}^t$:

$$\gamma_t(j,m) = \left(\frac{\alpha_t(j)\beta_t(j)}{\sum_{j=1}^{N}\alpha_t(j)\beta_t(j)}\right)\left(\frac{\omega_{jm}\mathcal{N}(\boldsymbol{\mu_{jm}}, \boldsymbol{U}_{jm})}{\sum_{m=1}^{M}\omega_{jm}\mathcal{N}(\boldsymbol{\mu_{jm}}, \boldsymbol{U}_{jm})}\right) \tag{5.30}$$

5.4 Training Data Set

In this work, experiments are conducted using Hidden Markov Model based target detection approach on two data sets: sense-through-foliage and sense-through-wall UWB radar data.

5.4.1 Sense-Through-Foliage Data Measurement

Sense-through foliage UWB data is from Air Force Research Lab[44]. The foliage penetration data are collected during late fall and winter with dense foliage. The experiment was constructed on a seven-ton man lift. The principle pieces of equipment secured on the lift are: Barth pulser, Tektronix model 7740B oscilloscope, dual antenna mounting stand, two antennas, rack system, IBM laptop, HP signal generator, custom RF switch and power supply and Weather shield (small hut). The pulse generator uses a coaxial reed switch to discharge a charge line for a very fast rise time pulse outputs. The target is a 1.5 meter trihedral metal reflector placed at 600 ft round trip distance from the base of the lift with the antenna 24 feet from the ground. Different data were taken from multiple positions with different azimuth

angels shown in figure X. Each data collection contains 16,000 samples for a total time duration of 0.8 microseconds at approximate sample rate of 20 Hz. Initially, the Barth pulse source was operated at low amplitude and 35 pulses reflected signal were averaged for each collection. This collection is referred as "poor" signal quality data. Later, good signal quality data were collected using higher amplitude pulses and 100 pulses reflected signals were averaged for each collection. This collection is referred as"good" signal quality data. In this experiment, we use the poor signal quality data set for training and testing data. Three different locations data are available for poor signal quality data. Each position includes 35 radar echoes for both target and no target cases.

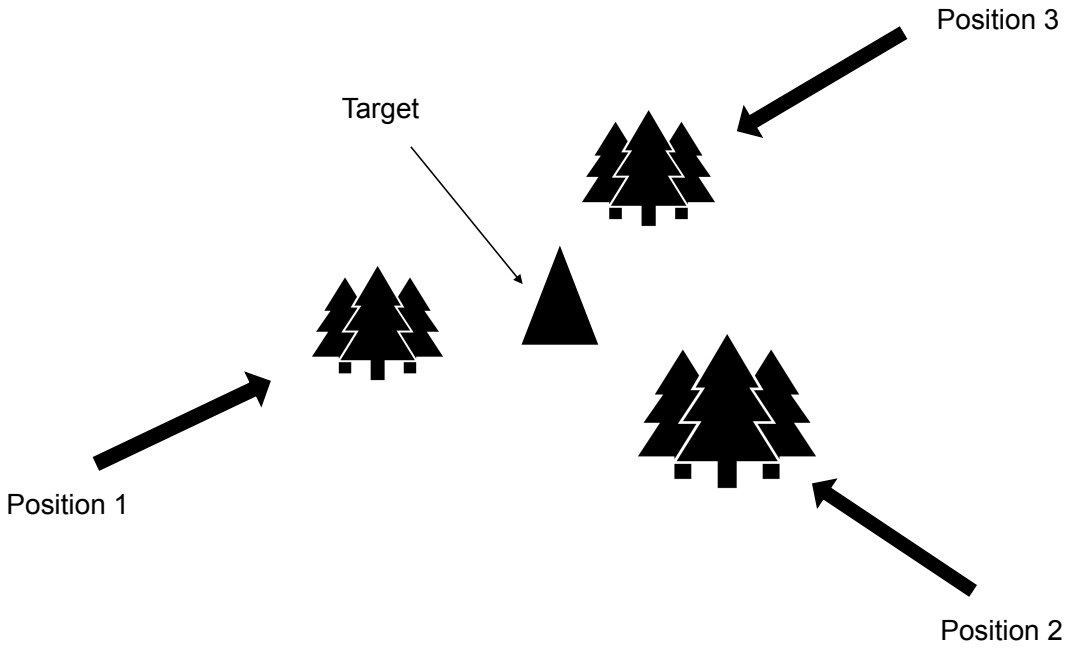

Figure 5.3. Radar echoes are collected from different positions.

5.4.2 Sense-Through-Wall Data Measurement

Sense-through-wall data is collected using P220 UWB radar with a center frequency of 4.3GHz and 10 dB bandwidth of approximately 2.3GHz. UWB radar works in monostatic mode where pulse waveforms are transmitted from a single omni-directional antenna. The received waveform are collected by another omni-directional antenna port. The measurement were taken from different locations with different types of walls [72] [73] [74]. Fig.5.4 and Fig.5.5 shows a human target stand behind a 30-cm thick gypsum wall with 6.5 feet to UWB radar on the other side. Fig.5.6 and Fig.5.7 shows human position behind a 4-cm wooden door at a distance around 7.5 feet from UWB radar. At each location, 100 radar scans are collected with stationary human target, without human target and human target with hand motion.

Figure 5.4. Location of the Human target on one side side of a thick Gypsum partition wall.

Figure 5.5. Location of the UWB radar on another side of a thick Gypsum partition wall.

5.5 Experimental Results

For sense-through-foliage poor quality signal data, the target appears at around 14,000 sample with a approximate on-site duration of 250 samples. To ensure that complete target information is included, we select 400 samples around 14,000 used for Hidden Markov Model training and testing for target and no target case. Then this 400 samples are evenly divided into different windows. Features are extracted and 13 features with minimum cross-correlation to other features are selected. The covariance matrix of selected 13 features are shown below:

Figure 5.6. Location of the Human target on one side side of a Wooden Door.

	$X1$	$X2$	$X3$	$X4$	$X5$	$X6$	$X7$	$X8$	$X9$	$X10$	$X11$	$X12$	$X13$	
	0.332	0.114	0.239	0.157	−0.090	−0.006	−0.035	0.191	0.003	−0.033	0.170	0.189	−0.012	$X1$
	0.114	0.324	0.234	−0.146	−0.032	−0.003	0.011	−0.028	0.020	−0.007	−0.166	−0.021	0.066	$X2$
	0.239	0.234	0.312	0.006	−0.069	−0.091	−0.012	0.106	0.010	−0.042	0.004	0.110	0.035	$X3$
	0.157	−0.146	0.006	0.329	−0.057	0.007	−0.111	0.201	−0.013	−0.052	0.292	0.193	−0.065	$X4$
	−0.090	−0.032	−0.069	−0.057	0.300	0.026	0.044	−0.207	0.027	0.143	−0.053	−0.185	0.050	$X5$
	−0.006	−0.003	−0.091	0.007	0.026	0.299	−0.007	−0.033	0.007	0.055	0.003	−0.036	−0.009	$X6$
	−0.035	0.011	−0.012	−0.111	0.044	−0.007	0.304	−0.078	0.023	0.123	−0.039	−0.076	0.038	$X7$
	0.191	−0.028	0.106	0.201	−0.207	−0.033	−0.078	0.322	−0.016	−0.148	0.192	0.316	−0.040	$X8$
	0.003	0.020	0.010	−0.013	0.027	0.007	0.023	−0.016	0.374	0.008	−0.020	−0.011	−0.002	$X9$
	−0.033	−0.007	−0.042	−0.052	0.143	0.055	0.123	−0.148	0.008	0.309	−0.007	−0.144	0.019	$X10$
	0.170	−0.166	0.004	0.292	−0.053	0.003	−0.039	0.192	−0.020	−0.007	0.324	0.180	−0.062	$X11$
	0.189	−0.021	0.110	0.193	−0.185	−0.036	−0.076	0.316	−0.011	−0.144	0.180	0.320	−0.038	$X12$
	−0.012	0.066	0.035	−0.065	0.050	−0.009	0.038	−0.040	−0.002	0.019	−0.062	−0.038	0.339	$X13$

For 35 radar echoes at each location, we use 20 sequences for HMM training and 15 sequences for testing. Finally, all three location data are combined together with a total of 105 sequences, 60 sequences are used for training and 45 sequences are used for testing. Baum-Welch algorithm are used to train two HMMs for target and no target denoted as λ_{Tar} and λ_{Notar}. Fig.5.8 and Fig.5.9 plots the Baum-Wech

Figure 5.7. Location of the UWB radar on another side of a Wooden Door.

learning curve of 2 states and 16 states HMMs training respectively, we can observe the log-likelihood reached a plateau indicates the algorithm converges.

To determine appropriate number of states is important for HMM to efficiently model the signal structure. However, there's no simple theoretically correct criteria to choose the number of HMM states. Increasing the number of states usually yields higher likelihood but comes with the penalty of increasing the number of parameters which may complicate the model and lead to overfitting. There are several states discovery criteria exists in current literature [71]. A commonly used approach is to comprehensively consider Akaike Information Criteria (AIC) and Beyesian Information Criteria (BIC) for states selection:

$$AIC = -2\ln(\hat{L}) + 2p \tag{5.31}$$

$$BIC = -2\ln(\hat{L}) + \ln(n)p \tag{5.32}$$

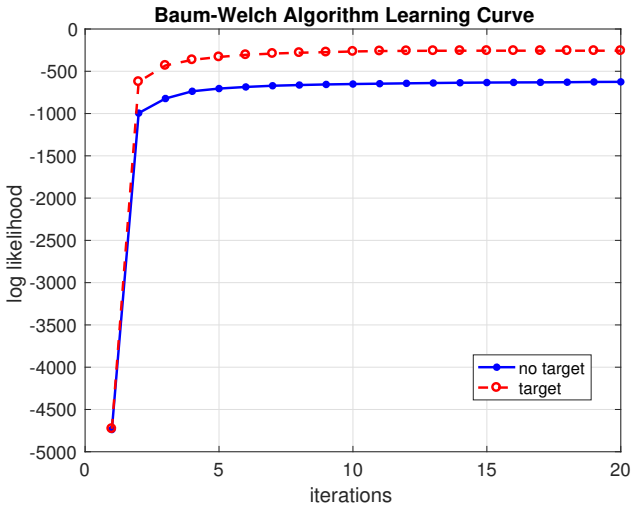

Figure 5.8. Baum-Welch training with 2 states HMM.

where $\ln(\hat{L})$ is the log likelihood, n is the number of data points and p is the number of estimated parameters. For Hidden Markov Model, the number of estimated parameters includes the elements of initial state distribution matrix π, state transition matrix A and Gaussian mixture observation matrix parameters $w_{jm}, \boldsymbol{\mu}_{jm}$ and $\boldsymbol{U_{jm}}$. So p can be calculated as follows:

$$p = N(N+1) + M(l^2 + l + 1) \tag{5.33}$$

The second terms of AIC and BIC score are the penalty terms increase with the number of parameters. Generally lower value of AIC/BIC indicates a good fit. For HMM, BIC generally has a larger punishment which leads to choosing more parsimonious models. Figure X shows the log likelihood and AIC/BIC scores with increasing number of states for sense-through-foliage HMM training.

From Fig.5.10 we can observe increasing likelihood with as number of states goes up. However, we can see prominent BIC score increasing, AIC has not increased much before the number of states increased to 6 as in Fig.5.11 This indicates a smaller number of states HMM suits better for radar signal modeling.

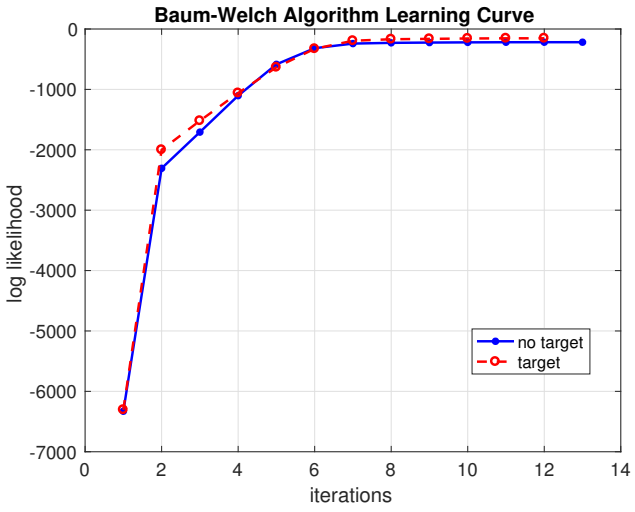

Figure 5.9. Baum-Welch training with 16 states HMM.

Then posterior likelihood of testing sequence O_{test} are calculated using both pre-trained models: $P_1 = P(O_{test} \mid \lambda_{Tar})$ and $P_2 = P(O_{test} \mid \lambda_{Notar})$, the decision rule of whether the testing sequence is target or no target is to compare the likelihood:

$$\begin{cases} P1 > P2 : Target \\ P1 < P2 : Notarget \end{cases}$$

The Baum-Welch algorithm requires initialization of model parameter drawn from uniform distributions which could affect the detection probability. In HMM training and testing, we use 100 Monte Carlo simulations to average out this random effect. Table X shows the confusion matrix of sense-through-foliage target detection results for three different positions and their combinations:

Position 1		
	No target	Target
No target	99.03%	0.07%
Target	11.33%	88.67%

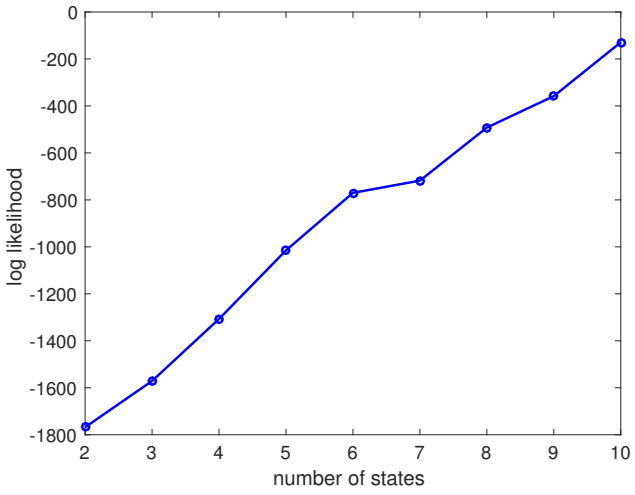

Figure 5.10. Loglikelihood increase by adding more number of states.

Position 2		
	No target	Target
No target	76%	24%
Target	17.57%	82.43%
Position 3		
	No target	Target
No target	82%	18%
Target	28%	72%
Position 1+2+3		
	No target	Target
No target	90.13%	9.97%
Target	33%	67%

Testing result shows Position 1 gives best probability of detection of 88% with a false alarm rate of 0.07%. The other two position data yields lower probability of detection with 82.43% and 72% and false alarm rate 24% and 18% respectively. The

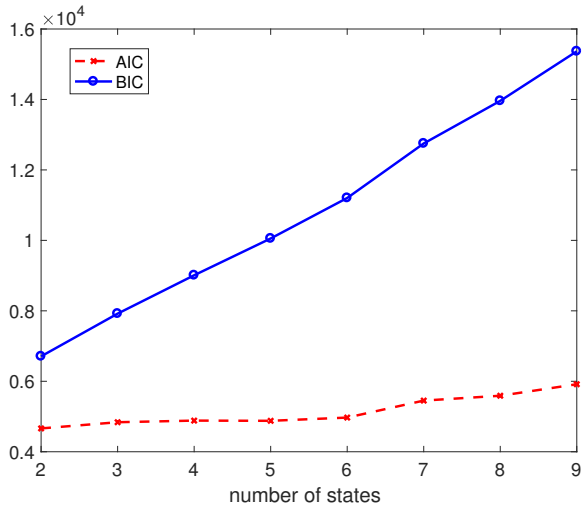

Figure 5.11. AIC/BIC score.

combination results shows 67% detection rate with 9.97% false alarm rate. Considering the experiment is conducted using poor signal quality radar echoes with lower transmitting power, the testing result is reasonable and could be further improved if signal quality is good. We can also find a lower probability of detection rate as three different location radar echoes are combined. The reason of performance degradation is that trihedral reflectors consisted of three electrically conductive surfaces used to reinforce the backscattered electromagnetic waves as the incoming waveforms from a certain direction and small variation of transmitting angels could cause low radar cross section.

Fig.5.12 shows the probability of detection and false alarm rate affected by the window size. It shows 20 and 25 samples window size gives best detection result and lowest false alarm rate. Intuitive explanation is that smaller window size means more observations of a given sequence are produced which provides more reliable estimation of parameters. However, when the window size is too small (e.g. 10 samples window size shown in Fig.5.12, the extracted features does not have any statistical significance.

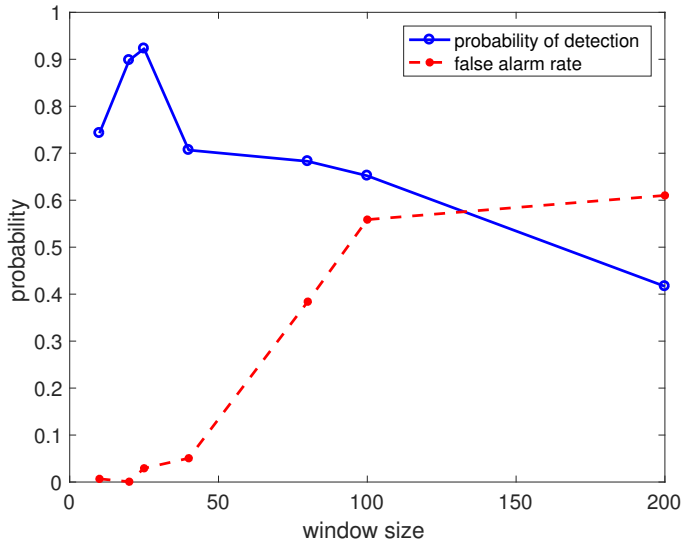

Figure 5.12. probability of detection and false alarm rate v.s. window size.

Fig.5.13 shows the probability of detection and false alarm rate affected by the number of states. The result shows gradually decreasing of probability of detection as the number of states increases. However, false alarm rate slowly increasing and remains at a comparatively low level even with large number of states. The testing result also confirms the fact that small number of states are more more suited to model UWB signal HMMs for target detection task.

Fig.5.14 shows the probability of detection and false alarm rate affected by the number of Gaussian Mixtures used to approximate observation probability density. Testing results also shows performance degradation by using more Gaussian Mixtures. However, probability of detection and false alarm rate remains stable when number of Gaussian Mixtures goes large.

For sense-through-wall human target detection, we choose to use Gypsum wall and wooden door data with radar scans of no human and stationary human behind

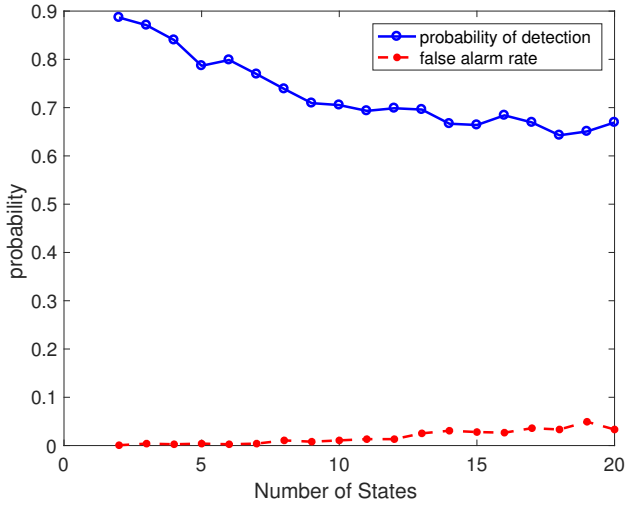

Figure 5.13. probability of detection and false alarm rate v.s. number of states.

walls. In order to reduce the clutter, difference between consecutive radar scans are used as HMM input:

$$\boldsymbol{Y} = \begin{matrix} scan(t) \\ \begin{bmatrix} sample1 \\ sample2 \\ \vdots \\ sampleN \end{bmatrix} \end{matrix} - \begin{matrix} scan(t+1) \\ \begin{bmatrix} sample1 \\ sample2 \\ \vdots \\ sampleN \end{bmatrix} \end{matrix}$$

In the sense-through-human target detection, we use $N = 2$ states, $M = 2$ Gaussian mixtures and window size $wn = 20$ as HMMs parameters. 2 HMMs regarding no human and stationary human are trained for human target detection. Table 5.1 shows 100% probability of detection and 4.17% false alarm rate with human target behind gypsum walls. Table 5.2 shows 94.87% probability of detection and 6.25% false alarm rate with human target behind wooden doors.

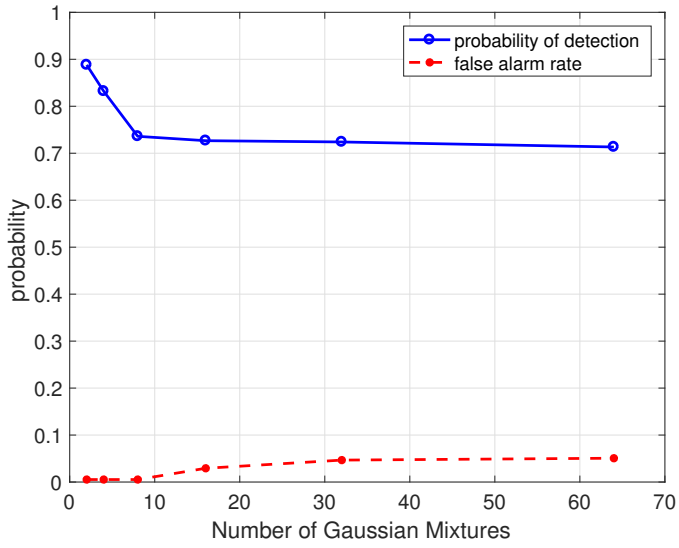

Figure 5.14. probability of detection and false alarm rate v.s. number of Gaussian Mixtures.

Gypsum Wall with 2HMMs		
	No human	Human
No Human	95.83%	4.17%
Human	0%	100%

Table 5.1. Detection result of human target behind gypsum walls

5.6 Conclusion

In this work, we use continuous HMMs to model the UWB radar signals for target detection. UWB radar signals around target location are windowed and feature vectors are extracted as distinctive observations sequences for HMMs training and testing. Sense-through-foliage and sense-through-wall experiments are conducted. Experimental results show that HMM has good performance in sense-through-foliage target detection in terms of probability of detection and false alarm rate. For sense-through-wall scenario, HMMs also show good capability to distinguish radar signals containing human target and no target. HMMs parameters are also investigated and

Wooden Door with 2HMMs		
	No human	Human
No Human	93.75%	6.25%
Human	5.12%	94.87%

Table 5.2. Detection result of human target behind wooden doors

results implicate that lower number states HMMs are better for UWB radar signal modeling and target detection task.

CHAPTER 6

Conclusions and Future Research

In this chapter, the conclusion of this dissertation is presented and followed by is the future work.

6.1 Conclusions

This dissertation includes massive MIMO performance analysis in terms of outage capacity and two different radar target detection approaches for radar target detection of UWB radar sensor networks.

Massive MIMO is a promising technology used for 5G networks. In Chapter 2, outage capacity of a single cell massive MIMO system are analyzed using scaling laws. Capacity scaling law firstly proposed by Gupta and Kumar as an asymptotic analysis method of large ad-hoc networks with certain increasing system parameters such as the number of nodes and infrastructures scales with network capacity. For 5G networks, massive MIMO system are implemented with large number of antennas to serve tens of users in each cell to improve capacity gain. Also base station densification is another technology aims to increase frequency reuse with smaller cells. In this system configuration, how capacity scales with increasing number of users, base stations and number of antennas is worth to look at. Theoretical uplink multi-user MIMO system are derived. Under favorable propagation condition, small scale fading is averaged out according to asymptotic orthogonality of the propagation matrix with increased base station antenna M. Large scale fading on throughput capacity is examined for both high SNR and low SNR case. Close-form outage throughput

capacity is derived. We proved that at low SNR, the infrastructure mode uplink outage capacity is $O\left(Mne^{-\sqrt{\log\left(\frac{1}{n}\right)\delta_\epsilon}}\right)$ $bit/s/Hz$. At high SNR, the infrastructure uplink outage capacity is $O\left(\frac{n}{b}\log(Mb) - \sqrt{\frac{n}{b}\delta_\epsilon}\right)$ $bit/s/Hz$. Increasing number of antennas at low SNR scenario yields better capacity gain compared to high SNR case. In Chapter 3, we derived the uplink Massive MIMO capacity using different outage criteria, e.g. asymptotic outage capacity and cell coverage ratio assuming log-normal large scale fading for both single-cell and multi-cell scenarios. Numerical result analysis show that shadow fading has significant impact on the performance. For single-cell system, imperfect CSI caused by channel estimation error suffers more from shadow fading effect. Performance degradation of multi-cell system are also observed with aggressive frequency reuse factor as shadow fading parameter increases.

Radar target detection is an important task for military and civil research and applications. Detection of target under strong background clutter is a challenging task. Chapter 4 investigates target detection using Empirical Mode Decomposition(EMD) based detection method. EMD is an data driven algorithm used for non-stationary signals analysis. In many areas like geophysics, economics, and engineering, EMD shows promising ability for time series analysis. In our work, we use EMD based approach for sense-through-foliage target detection. This method successfully detect target and high amplitude pulse are observed in IMF1 when UWB signal quality is good. When signal quality is poor, a single radar can not detect target using EMD approach. To improve the detection performance, A rake structure combined with multiple radar echoes are used to enhance signal to clutter ratio and from IMF2 of poor quality signal we can easily find similar target signature as the one in good quality signal scenario. From the experimental result, we also conclude that target return echo power is more concentrated in high frequency component as the background clutter is foliage. Machine learning show great success in many re-

search areas and real life applications recently. Chapter 5, Hidden Markov Model (HMM) based method are proposed for UWB radar target detection. In this work, HMMs are trained with extracted features from target and non target radar echoes for learning and testing. In sense-through-foliage target detection, we use poor quality signals collected from multiple radar locations for experiment. Results show that HMM method has 88% detection probability and 0.07% false alarm rate for position 1 data. Performance degrades as receivers has low effective radar cross-sections. In sense-through-wall human target detection, we observe high detection accuracy and low false alarm for stationary target. When hand motion involves, HMMs have lower detection accuracy and 20% to 30% stationary human target signals are misclassified as the ones with hand motions. We also show that small number of states HMMs have better performance for UWB radar signal modeling and target detection task.

6.2 Future Research

6.2.1 Target detection based on multi-modality decision fusion

Empirical Mode Decomposition has been widely used in 1D non-stationary and non-linear signal analysis. However, bidirectional EMD(BEMD) [47] [48] has been proposed these years for image processing. A 2D-sifting process can be used to decompose the image into different modes containing different frequencies of the image. These different modes show that the texture in each mode varies from fine and coarse. From different texture features obtained in each mode, the BEMD could be used in target detection in IR image [49] and sonar image [50] by separation of the target and background. In order to improve the target detection performance, 2D image data could be utilized to assist the target detection only using 1D data. EMD method can be used as an preprocessing method for 1D and 2D data fusion.

6.2.2 Extending HMM based approach for underwater target detection

In Chapter 5, HMM based target detection method shows good potential for reliable detector design. In the future, HMM can be applied to multiple UWB radar target detection and classification tasks. In our work, the detection tasks are basically focused on metallic and human target under different clutters. Sea clutter is another notorious environment made target detection difficult. HMM based target detection method can be applied to underwater environment to model sonar signals for target detection tasks.

REFERENCES

[1] F. Boccardi, R.W. Heath, A. Lozano, T.L. Marzetta, P. Popovski, "Five disruptive technology directions for 5G", IEEE Commun. Mag. 52 (2) (2014) 74-80.

[2] L. Lu, G.Y. Li, A.L. Swindlehurst, A. Ashikhmin, Z. Rui, "An overview of massive MIMO: Benefits and challenges", IEEE J. Sel. Topics Signal Process. 8 (5) (2014) 742-758.

[3] T.L. Marzetta, "Noncooperative cellular wireless with unlimited numbers of base station antennas", IEEE Trans. Wireless Commun. 9 (11) (2010) 3590-3600.

[4] E. Larsson, O. Edfors, F. Tufvesson, T. Marzetta, "Massive MIMO for next generation wireless systems", IEEE Commun. Mag. 52 (2) (2014) 186-195.

[5] J. Hoydis, S. ten Brink and M. Debbah, "Massive MIMO in the UL/DL of Cellular Networks: How Many Antennas Do We Need?," in IEEE Journal on Selected Areas in Communications, vol. 31, no. 2, pp. 160-171, February 2013.

[6] H. Q. Ngo, E. G. Larsson and T. L. Marzetta, "Energy and Spectral Efficiency of Very Large Multiuser MIMO Systems," in IEEE Transactions on Communications, vol. 61, no. 4, pp. 1436-1449, April 2013.

[7] X. Gao, O. Edfors, F. Rusek, F. Tufvesson, "Massive MIMO performance evaluation based on measured propagation data", IEEE Trans. Wireless Commun. 14 (7) (2015) 3899-3911.

[8] N. Bhushan et al., "Network densification: the dominant theme for wireless evolution into 5G," in IEEE Communications Magazine, vol. 52, no. 2, pp. 82-89, February 2014.

[9] N. E. Huang, Z. Shen, S. R. Long, M. L. Wu, H. H. Shih, Q. Zheng, N. C. Yen, C. C. Tung, and H. H. Liu, "The empirical mode decomposition and Hilbert spectrum for nonlinear and nonstationary time series analysis," Proc. R. Soc. London A, vol. 454, pp. 903?995, 1998

[10] F. Rusek et al., "Scaling Up MIMO: Opportunities and Challenges with Very Large Arrays," in IEEE Signal Processing Magazine, vol. 30, no. 1, pp. 40-60, Jan. 2013.

[11] D. Tse and P. Viswanath, *Fundamentals of Wireless Communication*, Cambridge University Press, 2005.

[12] P. Gupta and P.R. Kumar, "The Capacity of Wireless Networks", *IEEE Transactions on Information Theory*, vol.46, no.2, pp. 388-404, March 2000.

[13] B. Liu, Z. Liu, and D. Towsley, "On the Capacity of Hybrid Wireless Networks", *Infocom 2003* , vol. 2, pp. 1543-1552, April 2003.

[14] Xin Wang, Qilian Liang, "On the Throughput Capacity and Performance Analysis of Hybrid Wireless Networks over Fading Channels," IEEE Trans on Wireless Communications, vol. 12, no. 6, pp.2930-2940, June 2013.

[15] G. L. Stuber, *Principles of Mobile Communication*, Kluwer Academic Publishers, 2001.

[16] H. Q. Ngo, E. G. Larsson and T. L. Marzetta, "Aspects of favorable propagation in Massive MIMO," 2014 22nd European Signal Processing Conference (EUSIPCO), Lisbon, 2014, pp. 76-80.

[17] K. Zheng, S. Ou, and X. Yin, "Massive MIMO Channel Models: A Survey," International Journal of Antennas and Propagation, vol. 2014, Article ID 848071, 10 pages, 2014.

[18] M. Chiani, D. Dardari and M. K. Simon, "New exponential bounds and approximations for the computation of error probability in fading channels," in IEEE Transactions on Wireless Communications, vol. 2, no. 4, pp. 840-845, July 2003.

[19] E. Bjrnson, E. G. Larsson and M. Debbah, "Massive MIMO for Maximal Spectral Efficiency: How Many Users and Pilots Should Be Allocated?," in IEEE Transactions on Wireless Communications, vol. 15, no. 2, pp. 1293-1308, Feb. 2016.

[20] A. Yang, Z. He, C. Xing, Z. Fei and J. Kuang, "The Role of Large-Scale Fading in Uplink Massive MIMO Systems," in IEEE Transactions on Vehicular Technology, vol. 65, no. 1, pp. 477-483, Jan. 2016.

[21] A. J. Goldsmith, Wireless Communications. Cambridge University Press, 2005.

[22] M. S. Alouini and A. Goldsmith, "Area spectral efficiency of cellular mobile radio systems," 1997 IEEE 47th Vehicular Technology Conference. Technology in Motion, Phoenix, AZ, 1997, pp. 652-656 vol.2.

[23] J. Liang, Q. Liang and S. W. Samn, "Foliage Clutter Modeling Using the UWB Radar," 2008 IEEE International Conference on Communications, Beijing, 2008, pp. 1937-1941.

[24] S. Ayasli and L. Bessette, "UHF & VHF SAR phenomenology," presented at the Proc. PIERS, Workshop on Advances in Radar Methods, Baveno, Italy, July 20?22, 1998.

[25] A. Y. Nashashibi, K. Sarabandi, S. Oveisgharan, M. C. Dobson, W. S. Walker and E. Burke, "Millimeter-wave measurements of foliage attenuation and ground reflectivity of tree stands at nadir incidence," in IEEE Transactions on Antennas and Propagation, vol. 52, no. 5, pp. 1211-1222, May 2004.

[26] A. Y. Nashashibi and F. T. Ulaby, "Detection of stationary foliage-obscured targets by polarimetric millimeter-wave Radar," in IEEE Transactions on Geoscience and Remote Sensing, vol. 43, no. 1, pp. 13-23, Jan. 2005.

[27] Q. Liang, S. W. Samn and X. Cheng, "UWB Radar Sensor Networks for Sense-Through-Foliage Target Detection," 2008 IEEE International Conference on Communications, Beijing, 2008, pp. 2228-2232.

[28] Jing Liang, Qilian Liang, "Sense-Through-Foliage Target Detection Using UWB Radar Sensor Networks," (Elsevier) Pattern Recognition Letters, vol. 31, no. 11, pp. 1412-1421, August 2010.

[29] I. Maherin and Q. Liang, "A mutual information based approach for target detection through foliage using UWB radar," 2012 IEEE International Conference on Communications (ICC), Ottawa, ON, 2012, pp. 6406-6410.

[30] Ishrat Maherin, Qilian Liang, "Radar sensor network for target detection using Chernoff information and relative entropy", Physical Communication, Volume 13, Part C, December 2014, Pages 244-252.

[31] Ishrat Maherin, Qilian Liang, "Multi-Step Information Fusion for Target Detection using UWB Radar Sensor Network," IEEE Sensors Journal, vol. 15, no. 10, pp. 5927-5937, Oct 2015.

[32] Qilian Liang, Xiuzhen Cheng, Scott Huang, Dechang Chen, "Opportunistic Sensing in Wireless Sensor Networks: Theory and Applications", IEEE Trans on Computers, vol. 63, no. 8, pp. 2002-2010, August 2014.

[33] Qilian Liang, "Situation Understanding Based on Heterogeneous Sensor Networks and Human-Inspired Favor Weak Fuzzy Logic System", IEEE Systems Journal, vol. 5, no. 2, pp. 156-163, June 2011.

[34] Jing Liang, Qilian Liang, "Outdoor Propagation Channel Modeling in Foliage Environment", IEEE Trans on Vehicular Technology, vol. 59, no. 3, pp. 2243-2252, June 2010.

[35] Jing Liang, Qilian Liang, Sherwood Samn, "A Propagation Environment Modeling in Foliage", EURASIP Journal on Wireless Communications and Networking, Paper ID: 873070, vol. 2010.

[36] Qilian Liang, "Biologically-Inspired Target Recognition in Radar Sensor Networks", EURASIP Journal on Wireless Communications and Networking, Paper ID: 523435, vol. 2010.

[37] Qilian Liang, Xiuzhen Cheng, Sherwood Samn, "NEW: Network-enabled Electronic Warfare for Target Recognition", IEEE Trans on Aerospace and Electronic Systems, vol.46, no. 2, pp. 558-568, April 2010.

[38] Qilian Liang, Xiuzhen Cheng, "KUPS: Knowledge-based Ubiquitous and Persistent Sensor networks for Threat Assessment", IEEE Transactions on Aerospace and Electronic Systems,vol. 44, no. 3, July 2008.

[39] Z.Wu and N. E. Huang, (2009). "Ensemble empirical mode decomposition: a noise-assisted data analysis method. Advances in adaptive data analysis", 1, 1-41.

[40] Jian Guan, Jian Zhang, Ningbo Liu and Bao Li, "Time-frequency entropy of Hilbert-Huang transformation for detecting weak target in sea clutter," 2009 IEEE Radar Conference, Pasadena, CA, 2009, pp. 1-5.

[41] P. H. Chen, M. C. Shastry, C. P. Lai and R. M. Narayanan, "A Portable Real-Time Digital Noise Radar System for Through-the-Wall Imaging," in IEEE Transactions on Geoscience and Remote Sensing, vol. 50, no. 10, pp. 4123-4134, Oct. 2012.

[42] J. Li, L. Liu, Z. Zeng and F. Liu, "Advanced Signal Processing for Vital Sign Extraction With Applications in UWB Radar Detection of Trapped Victims in Complex Environments," in IEEE Journal of Selected Topics in Applied Earth Observations and Remote Sensing, vol. 7, no. 3, pp. 783-791, March 2014.

[43] P. Flandrin, G. Rilling and P. Goncalves, "Empirical mode decomposition as a filter bank," in IEEE Signal Processing Letters, vol. 11, no. 2, pp. 112-114, Feb. 2004.

[44] C. Dill, "Foliage Penetration (Phase II) Field Test: Narrowband ver- sus Wideband Foliage Penetration," Final Report of Contract Number F41624-03-D-7001/04, July 2005 to Feb 2006.

[45] I. Daubechies, "The wavelet transform, time-frequency localization and signal analysis," in IEEE Transactions on Information Theory, vol. 36, no. 5, pp. 961-1005, Sep 1990.

[46] G.Wang, X.Chen, F.Qiao, Z.Wu and N. E. Huang, (2010). "ON INTRINSIC MODE FUNCTION". Advances in Adaptive Data Analysis, 02, 277-293.

[47] Nunes, J.C. and Delchelle, E., 2009. "Empirical mode decomposition: Applications on signal and image processing". Advances in Adaptive Data Analysis, 1(01), pp.125-175.

[48] Linderhed, A., 2009. "Image empirical mode decomposition: A new tool for image processing". Advances in Adaptive Data Analysis, 1(02), pp.265-294. Vancouver

[49] Deng, H., Liu, J. and Li, H., 2009. "EMD based infrared image target detection method. Journal of Infrared", Millimeter, and Terahertz Waves, 30(11), pp.1205-1215.

[50] elebi, A.T. and Ertrk, S., 2010, April. "Target detection in sonar images using empirical mode decomposition and morphology", in Signal Processing and

Communications Applications Conference (SIU), 2010 IEEE 18th (pp. 760-763). IEEE.

[51] J. H. Reed, An Introduction to Ultra Wideband Communication Systems ser. Prentice Hall Communications Engineering and Emerging Technologies Series, NJ, Upper Saddle River:Prentice-Hall, 2005.

[52] M. G. Di Benedetto and G. Giancola, Understanding Ultra Wide Band Radio Fundamentals, ser. Prentice-Hall Communications Engineering and Emerging Technology. Englewood Cliffs, NJ: Prentice-Hall, 2004.

[53] L. R. Rabiner, "A tutorial on hidden Markov models and selected applications in speech recognition," in Proceedings of the IEEE, vol. 77, no. 2, pp. 257-286, Feb 1989.

[54] K. F. Lee and H. W. Hon, "Speaker-independent phone recognition using hidden Markov models," in IEEE Transactions on Acoustics, Speech, and Signal Processing, vol. 37, no. 11, pp. 1641-1648, Nov 1989.

[55] Y. Lecun, L. Bottou, Y. Bengio and P. Haffner, "Gradient-based learning applied to document recognition," in Proceedings of the IEEE, vol. 86, no. 11, pp. 2278-2324, Nov 1998.

[56] Christina Sauper, Aria Haghighi, and Regina Barzilay. 2010. Incorporating content structure into text analysis applications. In Proceedings of the 2010 Conference on Empirical Methods in Natural Language Processing (EMNLP '10). Association for Computational Linguistics, Stroudsburg, PA, USA, 377-387.

[57] S. Hahn et al., "Comparing Stochastic Approaches to Spoken Language Understanding in Multiple Languages," in IEEE Transactions on Audio, Speech, and Language Processing, vol. 19, no. 6, pp. 1569-1583, Aug. 2011.

[58] Hyeon-Kyu Lee and J. H. Kim, "An HMM-based threshold model approach for gesture recognition," in IEEE Transactions on Pattern Analysis and Machine Intelligence, vol. 21, no. 10, pp. 961-973, Oct 1999.

[59] M. Brand, N. Oliver and A. Pentland, "Coupled hidden Markov models for complex action recognition," Proceedings of IEEE Computer Society Conference on Computer Vision and Pattern Recognition, San Juan, 1997, pp. 994-999.

[60] P. J. Moreno and R. Rifkin, "Using the Fisher kernel method for Web audio classification," 2000 IEEE International Conference on Acoustics, Speech, and Signal Processing. Proceedings (Cat. No.00CH37100), Istanbul, 2000, pp. 2417-2420 vol.4.

[61] J. L. Gauvain and Chin-Hui Lee, "Maximum a posteriori estimation for multivariate Gaussian mixture observations of Markov chains," in IEEE Transactions on Speech and Audio Processing, vol. 2, no. 2, pp. 291-298, Apr 1994.

[62] L. A. Liporace, "Maximum likelihood estimation for multivariate observations of Markov sources", IEEE Trans. Informat. Theory, vol. IT-28, no. 5, pp. 729-734, 1982.

[63] B. H. Juang, "Maximum likelihood estimation for mixture multivariate stochastic observations of Markov chains", AT&T Tech. J., vol. 64, no. 6, pp. 1235-1249, July-Aug. 1985.

[64] B. H. Juang, S. E. Levinson, M. M. Sondhi, "Maximum likelihood estimation for multivariate mixture observations of Markov chains", IEEE Trans. Informat. Theory, vol. IT-32, no. 2, pp. 307-309, Mar. 1986.

[65] Pierre A Devijver. 1985. Baum's forward-backward algorithm revisited. Pattern Recogn. Lett. 3, 6 (December 1985), 369-373.

[66] A. J. Viterbi, "Error bounds for convolutional codes and an asymptotically optimal decoding algorithm", IEEE Trans. Informat. Theory, vol. IT-13, pp. 260-269, Apr. 1967.

[67] L. E. Baum, T. Petrie, "Statistical inference for probabilistic functions of finite state Markov chains", Ann. Math. Stat., vol. 37, pp. 1554-1563, 1966.

[68] L. E. Baum, "An inequality and associated maximization technique in statistical estimation for probabilistic functions of Markov processes", Inequalities, vol. 3, pp. 1-8, 1972.

[69] Hanchuan Peng, Fuhui Long and C. Ding, "Feature selection based on mutual information criteria of max-dependency, max-relevance, and min-redundancy," in IEEE Transactions on Pattern Analysis and Machine Intelligence, vol. 27, no. 8, pp. 1226-1238, Aug. 2005.

[70] R. Bakis, "Continuous speech word recognition via centi-second acoustic states," in Proc. ASA Meeting (Washington,DC), Apr. 1976.

[71] Gilles Celeux and Jean-Baptiste Durand. 2008. Selecting hidden Markov model state number with cross-validated likelihood. Comput. Stat. 23, 4 (October 2008), 541-564.

[72] Sukhvinder Singh, Qilian Liang, Dechang Chen, and Li Sheng, "Sense through Wall Human Detection Using UWB Radar," EURASIP Journal on Wireless Communications and Networking, vol. 2011, 2011.

[73] Ashith Kumar, Zhuo Li, Qilian Liang, Baoju Zhang, Xiaorong Wu, "Experimental Study of through-wall Human Detection using Ultra Wideband Radar Sensors," Elsevier Measurement, vol. 47, January 2014, pp. 869,879.

[74] Xiaoyang Li, Qilian Liang, Francis Lau, "Sense-Through-wall Human Detection Using UWB Radar With Sparse SVD," (Elsevier) Physical Communications, vol. 13, pp. 260-266, 2014.

BIOGRAPHICAL STATEMENT

Ganlin Zhao was born in Qufu, China, in 1989. He received her B.S. degree from Tianjin University, China, in 2012, and M.S. degree from University of Rochester, Rochester, USA, in 2014. He earned the Ph.D. degree from the University of Texas at Arlington in Electrical Engineering, in 2017. His research interests include UWB, target detection, radar signal processing and Massive MIMO systems.